

**Department of Physics and Astronomy
Heidelberg University**

arXiv:2508.16593v1 [physics.geo-ph] 8 Aug 2025

Bachelor's Thesis in Physics
submitted by

Constantin Schorling

born in Soltau (Germany)

2024

Estimating volumetric water content from electrical resistivity using a random forest model

This Bachelor's Thesis has been carried out by Constantin Schorling at the Institute of Environmental Physics in Heidelberg in cooperation with the University Center in Svalbard (UNIS)

Supervision and review:	Prof. Dr. Norbert Frank
Supervision and second review:	Prof. Dr. Werner Aeschbach
Supervision:	Knut Ivar Lindland Tveit, MSc.

Abstract

Background Accurately estimating volumetric water content (VWC) can greatly enhance the prediction of landslide risk. The standard approach involves using locally limited, invasive sensor measurements. Recently, however, electrical resistivity tomography (ERT) has emerged as a cost-effective, minimally invasive, real-time, indirect method of monitoring VWC. However, linking ER to VWC poses distinct challenges.

Purpose Random forest models were developed to estimate and predict VWC from ER. Spatially and temporally heterogeneous measurements were conducted to improve robustness and accuracy.

Methods The models were trained using 370–500 ER sensor measurements at depths of 10, 50, 150 and 190 cm. Precipitation and air temperature with a depth-dependent impact delay were introduced to simulate infiltration. The models were then validated at various locations, and their predictive capabilities were examined.

Results Including precipitation and temperature as parameters reduced the mean absolute error (MAE) by between 7.3% and 73.0%, depending on the depth. However, not all outliers could be eliminated. Delaying the model parameter depth-dependently reduced the maximum relative error (MaRE) by 14.7–56.0% and the mean relative error (MRE) to below 2.8%. Observed uncertainties for the top meter remained fairly constant. A 24-hour forecast revealed an MRE below 5% for all depths; however, outliers occurred more frequently. Nevertheless, models trained on data from one location failed to generalize to other locations. VWC tomography based on ERT revealed significant moisture bands at depths of one to two meters.

Conclusion VWC can be reliably predicted from ERT. However, validation of VWC from ERT in different locations revealed significant deficits. It is expected that an automated ERT training of models at various locations will eliminate these differences.

Contents

Abstract	V
Figures	IX
Tables	XI
1 Introduction	1
2 Basics	2
2.1 Permafrost characteristics	2
2.1.1 Permafrost structure	2
2.1.2 Physical properties	3
2.2 Electrical resistivity tomography (ERT)	4
2.2.1 Physical background	4
2.2.2 Data processing	7
2.3 Random forests	9
3 Materials and methods	10
3.1 Study area description	10
3.2 Observation period	14
3.3 ERT and sensor equipment and setup	16
3.4 GPS and height correction	17
3.5 Filtering and inversion scheme	17
4 Experimental Results	20
4.1 Overall ERT and sensor data processing	20
4.1.1 Basic ERT	20
4.1.2 Permafrost estimation	21
4.1.3 Sensor data	23
4.2 Finding the best correlation between electrical resistivity (ER) and volu- metric water content (VWC)	25
4.2.1 Random forest estimation	25
4.2.2 VWC estimation and forecast from ERT	30

4.3	Survey one: short-term temporal variations	33
4.4	Survey two: spatial overview and validation	33
4.5	Survey three: temporal long-term temporal variations	37
5	Discussion	39
5.1	ERT monitoring	39
5.1.1	ERT acquisition	39
5.1.2	Characterizing ERT and permafrost soil estimation	40
5.1.3	Sensor data	41
5.2	Estimating and predicting VWC from ER measurements	42
5.2.1	Influence of meteorological parameters	43
5.2.2	Influence of depth-dependent delays	44
5.2.3	Comparison of forecast to estimation	46
5.3	Testing the RF model for short temporal changes	47
5.4	Testing the RF model at various different locations	48
5.5	Active layer development throughout seasonal changes	49
6	Summary and Outlook	50
	Bibliography	52
	Appendix	60
A	Additional ERT	60
B	General ERT	61
C	Correlating VWC and ER	65
D	Short-term temporal variations	73
E	Spatial variations	78
F	Long-term temporal variations	79

Figures

1	ERT basics and background	6
2	Map of the Svalbard archipelago	10
3	Structural map of Longyearbyen with all study sites	12
4	Measurement setup for ERT and sensors	18
5	ERT on 28.08.2024 at study site 2	20
6	Virtual borehole from ERT	22
7	Active Layer and permafrost estimation	22
8	Long-term temperatures	24
9	Long-term VWC	24
10	Long-term ER	24
11	Model one, correlating ER and VWC	28
12	Model two, including temperature and precipitation	28
13	Model of best VWC estimation	29
14	Model of best 24 h VWC forecast	29
15	Depth-dependent delays	30
16	Comparison of VWC derived from ER and ERT	32
17	VWC tomography	32
18	ER and VWC data for ID S 3.12	34
19	VWC location validation with ID S 3.12	35
20	VWC training and est. with ID S 3.12	35
21	ERT from the different study sites across Longyearbyen	36
22	Seasonal long-term variations (ID2)	37

23	Correlation between VWC and VWC estimation	45
24	A-ERT	51
A.1	ERT for study sites 1, 3, 4	60
A.2	ERT for study sites 5, 6	61
B.3	ERT temperature calibration	65
C.4	MAE depending on delays for 10 cm and 50 cm model	68
C.5	MAE depending on delays for 100 and 150 cm models	69
C.6	MAE depending on delays for 190 cm models	70
C.7	38/48 h forecasts	71
D.8	Meteorological parameters for survey one without rain	73
D.9	Mean ER development for survey one without rain	73
D.10	ERT development for survey one without rain	74
D.11	VWC development for survey one without rain	75
D.12	Meteorological parameters for survey one with rain	76
D.13	Mean ER development for survey one with rain	76
D.14	ERT and VWC development for survey one with rain	77
E.15	Meteorological parameters for survey two	78
F.16	VWC development for survey three	79

Tables

1	Measurements at each study sites	13
2	Observation periods	15
3	ERT parameters	16
4	Mean ER from ERT for sensor spots	21
B.5	Mean ER by meter	61
B.6	ERT with means for dynamic depth ranges	62
B.7	ERT means at sensor positions	65
C.8	Best delay parameters for RF models	66
C.9	Delays for best VWC estimation	70
C.10	Delays for best VWC 24 h prediction	70
C.11	VWC comparison derived from sensors and ERT	72

1 Introduction

Rising global temperatures pose severe challenges, and the necessity for adaptation is becoming increasingly apparent [1]. This is particularly evident for Arctic regions, where the mean temperature increase is 3.8 times as high as observed globally between 1971-2021 [1, 2]. This yields an enhanced thawing of the prevailing permafrost. The active-layer – the upper most part of permafrost that seasonally freezes and thaws – thickens while the permafrost body underneath continuously melts [3, 4]. The permafrost shrinking presents challenges both globally and locally. The increased risk of debris flows and landslides threatens communities and infrastructure in its immediate vicinity [5].

Understanding and predicting impacts of these changes require a comprehensive assessment and monitoring of sub-surface structures. Today, there is a number of different geophysical methods employed to investigate lithosphere structures. Electrical resistivity tomography (ERT) can be used to indirectly obtain hydrological information of large areas. A two-dimensional resistance cross-section is generated, which can then be associated with hydrogeological properties calibrated with nearby boreholes and sensors [6, 7]. Especially for distinguishing active-layer and ground ice in permafrost this minimally invasive method can be useful as frozen and unfrozen areas vary in resistance in several orders of magnitude [8]. Furthermore, there is a strong correlation between volumetric water content (VWC), which is the ratio of water volume divided by the total sample volume, and ER offering the possibility to indirectly estimate VWC in a more cost-effective and extensive way [7, 9].

This thesis is part of the PermaMeteoCommunity Project [5] and focuses on the investigation of sub-surface structures using ERT in Longyearbyen, Svalbard, an Arctic settlement situated at 78°N 15°E [10]. The objective of the PermaMeteoCommunity Project is to develop a coupled permafrost and meteorological climate change response system, yielding an enhanced understanding and ability to predict and respond to permafrost-related changes in an Arctic environment.

The scope of the thesis includes a systematic contribution of ERT data observing active layer development as well as a novel approach to estimate and predict VWC from ER measurements (sensor and tomography) for enhanced landslide hazard assessment.

2 Basics

2.1 Permafrost characteristics

Sub-surface material and soil is considered permafrost if it remains at or below 0 °C for at least two consecutive years [3, 11]. The state can therefore solely be described thermally. As the temperatures, especially in polar latitudes, continue to rise [2, 12], the permafrost proceeds to thaw [13]. The stability of permafrost is determined almost exclusively by the ice content of the soil whereas the active layer – the layer above the permafrost which seasonally thaws and freezes – is also prone to volumetric water content (VWC) level elevations and sudden increases followed by subsidence and land detachments [14]. It is therefore a vital endeavor to quantify water and ice content seasonally, spatially and directly after heavy rainfalls [9, 14, 15] to detect areas of instability.

2.1.1 Permafrost structure

Vertically, permafrost soil can be characterized by three zones [16]: An upper seasonally freezing and thawing active layer, a transition zone underneath, in which the mean temperature is slightly negative but fluctuating, and an isothermic (perennially below zero) permafrost body. Below the lower limit of the permafrost base is a subpermafrost region with low positive temperatures.

The depth of the **active layer** is typically influenced by ground temperatures, but also several other environmental factors are relevant including topography, prolonging snow cover, vegetation, soil moisture and material [16]. The active layer thickness in Longyearbyen reaches up to 200-300 cm [4, 17]. Christiansen et. al [18] showed also for two sites in Svalbard (Adventdalen area and Ny-Ålesund) a continuous increase (0.6-1.6 cm/a, 5 cm/a) in the active layer thickness over the last 30 years. Another article [4] suggested a high influence of local parameters on the active layer thickness.

If a negative heat balance persists perennially, aggradation of the **transition zone** and also the **ground ice** increases [13]. Furthermore, a mean annual temperature decrease for deeper layers is observed [18]. Conversely, the permafrost volume decreases and its temperature increases with a positive heat balance. Thus, the shrinking or growing rate heavily depends on the annual mean heat balance [19]. Nevertheless, also other physical properties as heat capacity and permeability or a potential snow cover are significant [19].

2.1.2 Physical properties

Besides the stability, also other physical parameters of the sub-surface structures are heavily influenced by the active layer VWC. In the following section, the key parameter for observing water and ice as well as geological distributions with electrical resistivity tomography (ERT) will be discussed.

Electrical conductivity and resistivity

The electrical conductivity (EC) σ or resistivity (ER) ρ (reciprocal) of the soil is generally determined by three factors [6]. The electronic or metallic matrix conductivity (1) is influenced by the presence of free electrons within rocks (mostly ore minerals or carbons such as graphite). The in situ accumulation of water and ions from dissolved salts within the rock pores results in an electrolytical contribution (2) to the conductivity [20]. Conversely, the presence of air acts as an isolator, thereby reducing the conductivity [6]. The conductivity of clay-free rocks can be well approximated by the Archie's formula [21]:

$$\rho_0 = F \cdot \rho_w \cdot S^{-n} \quad (2.1)$$

where

$\rho_{0/w}$ = electrical resistivity of the sediment/pore water

F = formation factor

S/n = degree/exponent of saturation factor.

For clay rich conditions, a double layer forms between the pore water and the rock yielding current flow on the grain surfaces [6, 20]. An enhanced electrical conductivity due to interface contributions (3) is measured.

Rain, volumetric water content (VWC) and landslide risk

Heavy rainfall and subsequent infiltration can trigger dangerous slope failure due to a decrease of shear strength below a certain threshold [14, 9, 22]. Furthermore hydrological preconditions such as elevated moisture levels may reduce this threshold [14]. One way to measure moisture is based on the volumetric water content (VWC). Piciullo et al.

[23] summarized precipitation intensity, VWC elevation and sudden increases for various landslides. These thresholds are often multidimensional and require a sophisticated meteorological and soil observation.

2.2 Electrical resistivity tomography (ERT)

2.2.1 Physical background

ERT is one of the most commonly used geophysical techniques [8] and exploits the great heterogeneity of permafrost and active layer using basic electrical phenomena. In particular, the potential differences $\Delta\Phi$ and thus the apparent resistivity ρ is measured between metallic electrodes penetrating the ground minimally invasive with direct current [6]. As the electrical field is static and vortex-free ($\text{rot}\vec{E} = 0$) it is also a gradient field ($\vec{E} = -\nabla\Phi$) with a scalar potential Φ . The electrical field can be expressed with the electrical density \vec{j} or the electrical resistance σ as $\vec{E} = \frac{1}{\sigma}\vec{j} = \rho\vec{j}$. With this, the continuity equation:

$$\text{div}\vec{j} + \frac{\partial\rho_{el}}{\partial t} = 0 \quad (2.2)$$

yields

$$-\nabla \cdot [\sigma(x, y, z) \nabla \Phi(x, y, z)] = I \delta(x) \delta(y) \delta(z) \quad (2.3)$$

for a point source electrode at $(0, 0, 0)$ [24]. Assuming a homogeneous, endless ground confined by a straight surface (yielding a perfect half space), the radial potential between a feeding electrode A and a measuring electrode M is given by

$$\Phi(r) = \rho \frac{I}{2\pi r} \quad (2.4)$$

with the distance $\overline{AM} = r$ [6]. For common setups a current ($\pm I$) is applied between two feeding electrodes A and B while the potential difference (voltage) is measured between two other electrodes M and N (see Fig. 1 A). All individual potentials superimpose and result in the Neumann equation [6]

$$U = \Delta\Phi = \rho I \left[\frac{1}{2\pi} \left(\left(\frac{1}{r_1} - \frac{1}{r_3} \right) - \left(\frac{1}{r_2} - \frac{1}{r_4} \right) \right) \right] = \frac{\rho I}{K}. \quad (2.5)$$

Setting the distance dependent term K and current I and measuring the voltage U yields the resistivity ρ

$$\rho = \frac{UK}{I}. \quad (2.6)$$

For simplicity, a point shaped electrode was assumed [20]. The potential for a rod current source requires a small correction, however this is negligible at distances exceeding 50 cm ($< 5\%$ deviation) [25].

Soil inhomogeneities and the transition from active layer to permafrost result in different electrical conductivities and therefore change equation 2.4. The current is refracted at material boundaries according to the general law of refraction $\frac{\rho_1}{\rho_2} = \frac{\tan(\theta_1)}{\tan(\theta_2)}$ [6].

Wenner array

The electrodes can be controlled individually depending on the desired resolution. In this thesis, a Wenner array was chosen as it provides a high Signal-to-Noise-Ratio and layer resolution [6]. The feeding electrodes (A, B) surround the measurement electrodes (M, N) with an equidistant electrode spacing $r = n \cdot a$ ($n \in \mathbb{N}$) for all electrodes (see Fig. 1 A). Given that $r_1 = r_4 = an$ and $r_2 = r_3 = 2an$, this yields $\rho = 2\pi a \frac{U}{I}$ [20].

After the first measurement using the first four electrodes, the feeding and read out is shifted altogether by one electrode. Shifting the electrode tasks is continued until the last electrode (layer 1 is then finished). Thereafter, the distance between each utilized electrode is increased by a , yielding an electrode spacing of $2a$ for the second layer (see Fig. 1 B). This is continued until the \overline{AB} spacing is larger than the array and the lowest reachable layer n is observed. In Fig. 1 C and D for the first two layers the current flow lines and equipotential lines are displayed in black and heat colors, respectively. The final result is obtained by combining all separate measurements constructively [6]. The Wenner array is superior in lateral resolution compared to other array types [6]. However, it lacks depths resolution. The initial electrode spacing can be varied to gain near-surface resolution with shorter spacing or deeper investigations with wider spacing [8]. The exploration depth is constrained by the array length and can be approximated for the Wenner array as $0.17\overline{AB}$ [6]. Other commonly used arrays like Dipole-dipole, Wenner-Schlumberger or Gradient feature different sensitivity profiles and penetration depths as they have other electrode configurations [8].

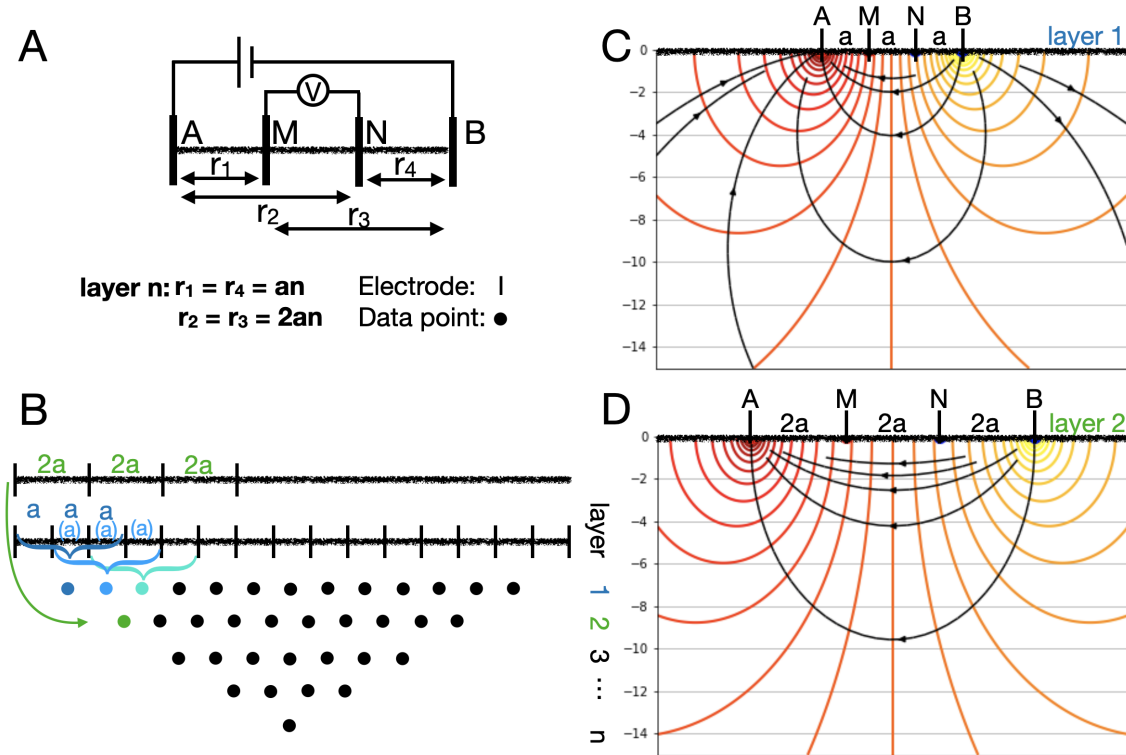


Figure 1: A characterization of Wenner array under assumption of homogeneous ground; A: Schematic of the feeding and measuring electrodes and intermediate distances, B: The overall data acquisition and penetration depth, C: The current flow lines (black) and equipotential lines (heat colors) for layer one with electrode spacings of a , D: Layer two, electrode spacing: $2a$; A is adapted from [20] and B from [6].

Data acquisition prerequisites

To generate statistically relevant data, a series of measurements is usually recorded successive as a stack [8] avoiding electrode location errors because of repositioning.

There are multiple prerequisites for obtaining useful data. After choosing a specific ERT array length and type, all electrode positions need to be recorded with GPS to facilitate further data evaluation [6, 8]. Other external influences as topography, meteorological circumstances and surface cover must be addressed and considered for evaluation. When measuring the resistivity, it is crucial to guarantee a sufficient galvanic coupling between all electrodes and the soil [26]. Depending on the above mentioned factors it can be challenging to secure this. Prior knowledge of soil conditions is generally not required, but

may be valuable for selecting appropriate currents to produce voltage magnitudes within a detectable range [8].

2.2.2 Data processing

The acquired data is first arranged in a pseudosection [27], a rough schematic of the sub-surface resistivity profile. To obtain a more accurate description of the resistivity and potential soil composition, a series of data analysis must be conducted.

Data filtering

The propagation of errors introduced by systematic measurement faults is mitigated using three filtering processes [8]. In the first step, all data points indicating negative voltages or currents are removed. Furthermore, if multiple surveys were performed (stacking), data revealing a variance between the measurements above an adjustable threshold are also eliminated (e.g. $> 5\%$ [9]). The same applies to data that deviate very strongly from all others. Thresholds are often chosen to be around 9 times the standard deviation [8]. Secondly, at each depth a horizontally sliding array of each five values is used to calculate for every position the mean value and detect and delete anomalies. The threshold for acceptable deviations from the mean is approx. 5-10% [8]. Lastly, an electrode filter eliminates all data points associated with electrodes, from which in previous steps, much data was removed (above an adjustable percentage).

Inversion

After filtering the measured data a first resistivity model (step one) is generated. A heuristic approach is employed setting an initially homogeneous model m_0 modified by prior knowledge [20]. Thereafter, with forward modeling (step two), the partial differential equation 2.3 is solved numerically using the finite difference method (FDM) [28] leading to an ambiguous pseudosection and adapted model parameter m .

Furthermore, an objective function $\phi(m)$ (step three) is calculated incorporating both, the data misfit ϕ_d and the model misfit ϕ_m [8]. A deviation description from model to the data (ϕ_d) is combined with a smoothness constraint (ϕ_m) ensuring realistic values. A

regularization parameter β is introduced to allow for a weighting of the constraint [8].

$$\phi(m) = \phi_d(m) + \beta \phi_m(m_0, m) \quad (2.7)$$

$$= \|d_{meas} - d_{model}(m)\|_p + \beta \|d_{model}(m_0) - d_{model}(m)\|_q \quad (2.8)$$

The data is delineated by d , while p and q describe the order of the norm. L1, L2 or a combination are the common for both [20, 29, 30]. Loke et al. [31] argued that employing an L1 norm for data misfit modeling yields sharper boundaries as it penalizes outliers less. Furthermore, Herring et al. [8] conclude its benefits especially for permafrost investigations as the lateral boundaries of frozen and unfrozen ground is considered sharp. This was also shown by Glazer et al. [29] who investigated spatial permafrost distributions in Spitsbergen.

To minimize $\phi(m)$ the model parameters m are varied (step four). Commonly, a form of the gradient based Gauss-Newton algorithm or Levenberg-Marquardt algorithm (LMA) [20, 12, 32, 33] is used to update the parameters. The LMA shifts the initial parameters depending on the Jacobian matrix J_r and residuum r .

$$m_{k+1} = m_k - (J_r^T J_r + \lambda I)^{-1} J_r^T r(m_k) \quad (2.9)$$

$$r = d_{meas} - d_{model}(m) \quad (2.10)$$

Moreover, a damping coefficient λ is introduced yielding the Gauss-Newton algorithm for small values of λ and an iterative gradient descent for high values [33]. Thus, λ should initially be chosen large and decreasing with lower model-data-deviations [12, 33].

Calculating Jacobian matrices for each iteration of m_k is time-consuming. Loke and Barker [24] introduced a so called quasi-Newton method to reduce the computation significantly. First, the Jacobian matrix J_0 for the initial homogeneous model m_0 is solved analytically. All following Jacobians are approximated iteratively, thereby obviating the necessity to solve all differentials exactly [24]. However, especially for large resistivity contrasts Loke and Dahlin [32] showed a significant accuracy drop for quasi-Newton compared to Gauss-Newton. For such cases – including permafrost – a potential compromise between accuracy and computing effort might be achieved, by combining two recalculations of the exact Jacobian in the first iterations and then approximating subsequent ones [20, 24].

Steps three and four are repeated iteratively until a terminating convergence threshold is reached. This is not necessarily a global minimum of the objective function as multiple solutions to the nonlinear least squares problem exist and depend on the initial parameters [8]. Further, the initial parameters can also be varied finding better convergences [33].

The converged model provides insights about sub-surface resistivities and can help to understand the underlying structures. Nevertheless, it is necessary to obtain further field investigations, including but not limited to sensors, surface observations, borehole analysis, ground-penetrating radar and frost table depths [8]. The combination of multiple survey forms then yields a sophisticated understanding of the sub-surface [15, 9, 29, 34].

2.3 Random forests

For the correlation of electrical resistivity (ER) and volumetric water content (VWC) a random forest regressor is used in this thesis. The regressor consists of n decision trees [35]. For each tree an input space with VWC as weights and the observed features (ER, temperature, precipitation) is split into different regions by successive statements about the features. The splits are chosen to minimize the mean square error of VWC prediction and measurement. [36]. At each node, the best feature and the best value of the feature are chosen as the split. For a random forest, the n regression trees are constructed from subsets of the input space, randomly selected with replacement, and with i randomly selected features for each node. The prediction for VWC is then the mean of the predictions from all trees (bagging) [37].

The concept of trees is generally easy to interpret, since only logical rules (for example: ER value $< 300 \Omega \cdot m$; yes: VWC value $= 0.24 \text{ cm}^3 \text{ cm}^{-3}$; no: VWC value $= 0.22 \text{ cm}^3 \text{ cm}^{-3}$) are derived as decisions, and an automatic selection of these decisions is performed, which is robust to outliers [35]. Nevertheless, a tree is often unstable and of high variance due to a greedy minimization of the splits. This is taken into account by averaging many trees for the random forest regression, which leads to better accuracy [35].

3 Materials and methods

3.1 Study area description

The study area is located in Longyearbyen ($78^{\circ}13'N$, $15^{\circ}28'E$ [34]) on the Spitsbergen island (Svalbard, Norway) [10]. The study area in central Svalbard is located in the con-



Figure 2: Map of the Svalbard archipelago.

tinuous permafrost region [16, 38]. Typical permafrost thicknesses in Svalbard range from few meters to more than 100 m in valleys and up to 450 m at mountains around Longyearbyen [39, 40]. Active layer thicknesses reach approx. 200-300 cm in Longyearbyen [4, 17]. Spitsbergen is influenced by a polar-tundra climate [41] according to the Köppen-Geiger classification. The annual mean air temperature in Longyearbyen (Airport) for the observation period 1971-2000 was approx. $-6^{\circ}C$ thus well below $0^{\circ}C$ [17].

Nevertheless, a continuous increase particularly during the most recent decades (1.0 °C-1.2 °C per decade between 1980-2010) is visible and an even more drastic rise is observed comparing the winter seasons [17, 42]. The 30-year temperature mean in Longyearbyen was -3.9 °C in 2018 [34]. Further drillhole measurements in Svalbard suggested a continuous mean ground temperature increase of 0.06-0.15 °C/a and 0.07-0.08 °C/a between 2008 and 2016 for depths of 10 m and 20 m, respectively [17].

As Longyearbyen is surrounded by plateau mountains up to 500 m a.s.l. a natural rain shadow is created [17] and the mean annual precipitation is about 200 mm for the time period 1971-2000 in the Longyearbyen area. Approximately half of the yearly precipitation occurs as snow in winter and spring [42]. Furthermore, since 1912 the mean annual precipitation increase was about 2%-4% per decade [17, 42] with higher increases in autumn. For a sophisticated investigation other parameter as topography, prolonging snow cover, vegetation, soil moisture and material need to be consolidated [16].

Six test areas (see Fig. 3 and Tab. 1 for further details) were selected as representatives for present geomorphological and slope conditions in Svalbard as well as in other Arctic locations [34]. Further, all locations are situated on slopes and directed along the gradient (see also Fig. 3) except ERT 1.1, which is situated transverse it.

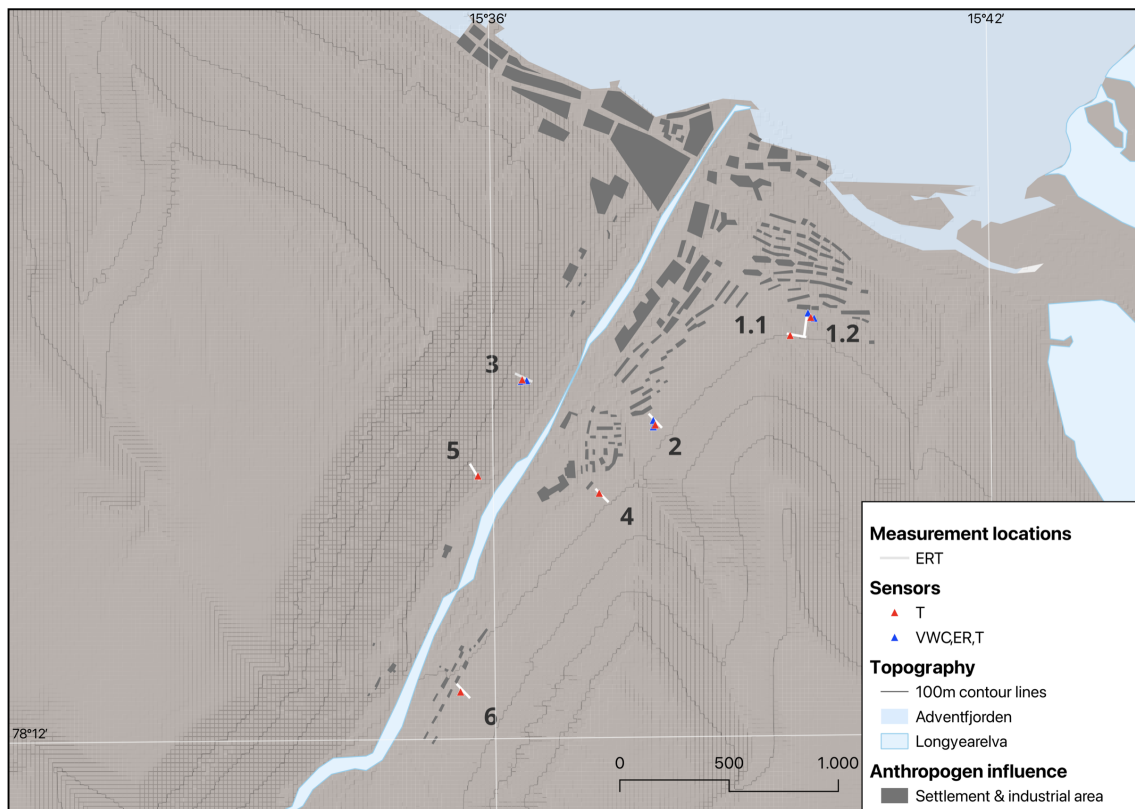


Figure 3: A structural map of Longyearbyen showing settlements and height contours. The study areas are marked, T means temperature while VWC, ER and T depict combined known abbreviations.

The investigated slopes face the settlements and pose a considerable danger on nearby infrastructure and buildings in forms of avalanche, debris flow and landslide risk.

At study area 1 two ERT lines were installed to cover a broader slope area. The northern slope of the Sukkertoppen mountain above the highest building line was selected for this study site as in October 2016 a landslide was nearly caused after a warm and wet summer, followed by a heavy rainfall event [43]. This is also visible on aerial pictures taken from that area. Study area 1 covers approximately 0.8 ha and ends about 20 m above the first houses. Line 1.1 was chosen perpendicular and line 1.2 parallel to the slope direction.

Table 1: Specifications for the study sites. T-depths includes the depths [0, 10, 20, 40, 60, 80, 100, 120, 140, 160, 180, 200, 250, 300, 350, 400] cm while T stands for temperature measurements which is measured at each sensor location.

Location ID	Start Coordinates	End Coordinates	Length [m]	Elevation range [m a.s.l.]
1.1	78° 12' 59,39" N 15° 39' 34,04" E	78° 12' 58,91" N 15° 39' 46,39" E	80	98.53 - 97.46
1.2	78° 12' 59,20" N 15° 39' 45,91" E	78° 13' 02,22" N 15° 39' 47,94" E	100	96.20 - 64.77
2	78° 12' 45,82" N 15° 38' 01,64" E	78° 12' 47,66" N 15° 37' 53,40" E	80	77.28 - 58.42
3	78° 12' 53,86" N 15° 36' 17,39" E	78° 12' 52,79" N 15° 36' 28,17" E	80	82.66 - 60.41
4	78° 12' 34,91" N 15° 37' 22,53" E	78° 12' 36,65" N 15° 37' 14,38" E	80	93.47 - 65.94
5	78° 12' 40,51" N 15° 35' 43,62" E	78° 12' 38,40" N 15° 35' 49,82" E	80	94.56 - 72.40
6	78° 12' 06,15" N 15° 35' 40,98" E	78° 12' 08,03" N 15° 35' 32,71" E	80	124.11 - 108.67

Location ID	Coordinates	Ground height [m a.s.l.]	Depths [cm]	Measurements
S 1.11	78° 12' 59,14" N 15° 39' 35,65" E	99,46	T-depths	T
S 1.21	78° 13' 02,44" N 15° 39' 48,68" E	62,45	50, 100, 150	VWC, ER, T
S 1.22	78° 13' 01,91" N 15° 39' 48,20" E	67,26	10, 90, 140, 190	VWC, ER, T
S 2.1	78° 12' 46,37" N 15° 37' 58,12" E	101,10	10, 50, 100, 150, 190	VWC, ER, T
S 2.2	78° 12' 46,81" N 15° 37' 56,07" E	64,73	50, 100, 150, 160	VWC, ER, T
S 3.11	78° 12' 53,29" N 15° 36' 22,66" E	69,89	T-depths, 450, 500	T
S 3.12	78° 12' 53,29" N 15° 36' 22,66" E	69,89	10, 50, 100, 150, 200	VWC, ER, T
S 3.2	78° 12' 52,97" N 15° 36' 25,08" E	64,58	10, 50, 100, 150	VWC, ER, T
S 4	78° 12' 36,13" N 15° 37' 16,46" E	73,73	T-depths excluding 350 and 400	T
S 5	78° 12' 38,86" N 15° 35' 49,02" E	74,78	T-depths, 450, 500, 550, 600, 650, 700	T
S 6	78° 12' 06,94" N 15° 35' 34,88" E	114,73	T-depths, 450	T

3.1 Study area description

Next to line 1.2, temperature sensors were already measuring every 6 h at depths between 10 cm and 400 cm. Further down, besides line 1.1 VWC, EC and temperature sensors in depths of 10 to 190 cm were just installed in early October 2024.

Site 2 was chosen on the southwards slope of Sukkertoppen. Nearby this measurement station there was an avalanche incident in December 2015 displacing several houses and taking two lives [44]. Thereupon, multiple fences on the slopes of Sukkertoppen and an avalanche embankment underneath were build to prevent avalanches, landslides and mud slushes in the most endangered regions. For further ground observation especially connected to landslides, location 2 was chosen on the slope approximately 30 m above the very top houses and about 200 m north-east to Vannledningsdalen. There, temperature, VWC and EC sensors were already installed in December 2023 in depths of 10 cm to 190 cm. The subsurface for the top 30 m of the ERT line consists of colluvial material, heterogeneous, loose and unconsolidated rocks. Below this, the geomorphology is dominated by solifluction, a slow mass wasting process due to freeze-thaw action [45, 46].

Study sites 3 and 5 are located west of the village on the slopes of Sverdruphamaren. These sites are also characterized by colluvial material (the top 20 m at site 5) and solifluction (the top 60 m at site 3). The contact resistance for site 5 (and 6) was significantly higher (mean around 2 k Ω , sometimes up to 5 k Ω) compared all other sites (0-2 k Ω) because of the colluvium. Site 5 is additionally monitored by temperature sensors down to 700 cm, at site 3 temperature, VWC and EC sensors are installed at two locations.

Study site 4 is located about 30 m above the Haugen district. Continuous temperature data for depths of up to 300 cm is available here.

Study site 6 is located on the south-eastern slope above Nybyen, a district of Longyearbyen, The ERT line was constructed about 15 m above the upper most houses next to the temperature sensors (down to 450 cm). This slope is completely dominated by colluvium. The contact resistance was correspondingly high at 2 – 4 k Ω as site 5.

In general, the measuring positions were selected based on the occurrence of the greatest number of avalanches and landslides with damage to infrastructure or people in the recent years.

3.2 Observation period

The overall investigation period began in mid August 2024 and ended in late October 2024. Three surveys at different locations and times were conducted to assess spatial,

long-term temporal and short-term temporal variations.

The short-term variation observations (survey one) were designed to test the influence of small mean temperature fluctuations, but primarily precipitation variations on the accuracy and robustness of the models. Therefore, two time intervals were chosen, one without significant rainfall and one shortly after a heavy rainfall event after which resulting infiltration was to be observed. Survey one was carried out in early October to ensure air temperatures above zero degrees.

The spatial observation survey (survey two) encompasses seven single measurements performed from 02.09.2024 until 06.09.2024. The temporal proximity of these measurements was designed to minimize seasonal temperature changes as well as precipitation deviations. To observe the highest depth dependent variations, i.e. the highest active layer thickness, the measurement period was set to early September.

Long-term seasonal changes especially in the uppermost active layer were observed by conducting weekly measurements (survey three). In total 12 weeks were investigated resulting in a time laps ranging from summer (August) until the complete freezing of the ground and a termination of the measurement period in the beginning of winter (October).

In Tab. 2 all surveys and dates of measurements are listed.

Table 2: Three different surveys were performed to guarantee insights over short-term temporal variations (survey 1), spatially (survey 2) and long-term temporal variations (survey 3).

Survey	Location	Time	Frequency
1	2	29.08.-01.09.2024	daily: 6:30, 12:30, 18:30
	2	06.09.2024	9:00, 12:00, 15:00
2	1.1	03.09.2024	once
	1.2	03.09.2024	once
	2	04.09.2024	once
	3	04.09.2024	once
	4	05.09.2024	once
	5	05.09.2024	once
	6	02.09.2024	once
3	2	14.08.-30.10.2024	weekly

3.3 ERT and sensor equipment and setup

The ERT were conducted using an ABEM Terrameter SL 2 (Guideline Geo AB, Sweden) driven by an embedded ARM 9 processor and powered by an external car battery. For each ERT 81 rod electrodes (40 cm length, 3.5 cm diameter) were placed at 1 m equidistance and were used with a Wenner array to ensure high lateral resolution, but also to obtain some depth resolution into the permafrost. They were hammered about 10 cm into the ground to achieve sufficient galvanic coupling. Additional salt water was introduced for electrodes with high contact resistances, which was found efficient. For study site 1.2 a 100 m line was set up with an equal spacing. The measurement of 445 points took around 2 h.

For all sites, both resistivity and induced polarization were measured while only resistivity was currently used for the analysis. The number of stacking was set from 2 to 4 which ensures small errors – the standard deviation in a stack divided by the mean value for a data point was set to 1% – but also keeps the measurement time short. The delay and acquisition time were also set to achieve a good compromise between above criteria. The transmit parameters were chosen to secure the instrument while improving the signal-to-noise ratio. All important settings for receiving and transmitting are summarized in Tab. 3.

Table 3: Important receive and transmit parameter used to obtain the ERT.

Receive		Transmit	
Measurement mode	Res, IP	Min Current	1 mA
Min Stacking	2	Max Current	1000 mA
Max Stacking	4	Max Power	250 W
Error limit	1.0 %	Max output voltage	600 V
Delay time	0.6 s	Load variation margin	10%
Acquisition time	0.4 s		
Power line frequency	50 Hz		
Sample rate	1000/1200 Hz		

To install the sensors, a hole was excavated and sensors were inserted at different depths. The sensor needles were placed horizontally to allow a more discreet depth for all sensors. VWC is measured by applying a 70 MHz oscillation and a read out of the subsequent

charge time of the 1,010 mL sensitive volume around the sensors. The charge time is proportional to the dielectric properties and VWC of the substrate. A thermistor in the center needle is used for temperature measurement. The electrical conductivity (EC) is obtained by running an alternating current between the outermost needles and gauging the resistance between them. The ER as reciprocal EC is then obtained. All sensors measure every 6 h and are connected to a data logger. An already existing sensor setup was used for the research described in this thesis.

3.4 GPS and height correction

The GPS data acquisition for the sensor points and the individual electrodes of all ERT was recorded with a Leica Viva GS16 GNSS rover (Leica Geosystems AG, Switzerland). Subsequent corrections were performed by combining the individual data further improved the accuracy. The achieved average accuracy was within centimeter range. However, the height data of the electrodes showed large fluctuations of neighboring electrodes, which was not realistic. For this reason, the coordinates were combined with a digital elevation model (DEM) for height calculations. A DEM developed from the Norwegian Polar Institute [10] with a 2.5 m resolution was used. The resulting heights were interpolated and flattened by taking the average of three adjacent electrodes and applying it to the center electrode.

In an effort to better illustrate the layering and infiltration, the analysis was applied to the non-height corrected ERT. The data points were interpolated linearly in a trapezoidal pattern. Nonetheless, as the slope is not perfectly linear, errors are introduced.

3.5 Filtering and inversion scheme

The recorded data points were processed further using the open-source software ResIPy (version: 3.3.5) [47] and the previously determined topography was applied. Three filters were employed to remove outliers.

Initially, erroneous data points, defined as those with transfer resistance values less than zero ohms, were identified and removed. Additionally, data points exhibiting unusually high deviations ($> 10\%$) from the transfer resistance values of neighboring points within a given layer were also filtered out. The same methodology was employed for apparent

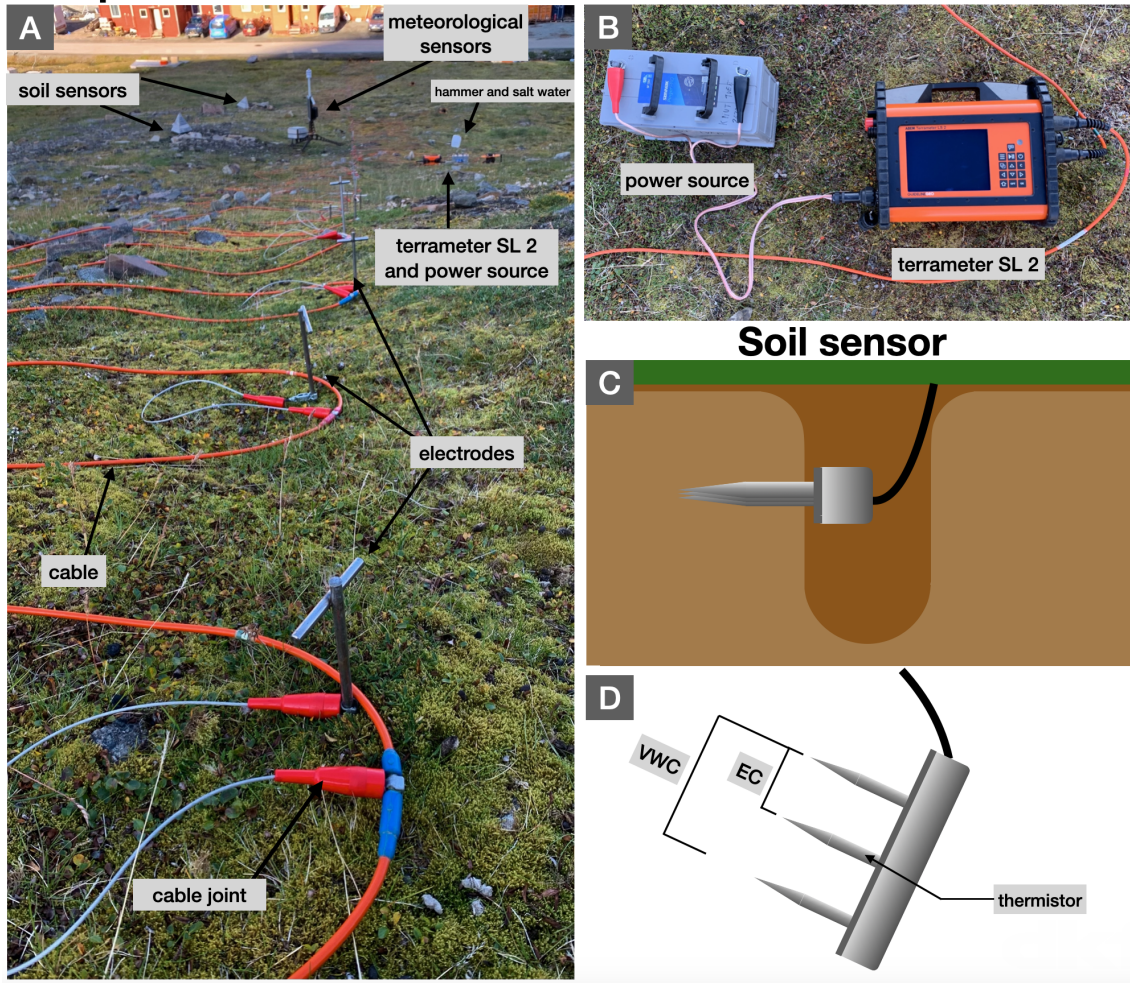


Figure 4: The overall measurement set up including sensor measurements and ERT; A: The electrodes were connected by cable joints to the cable and the Terrameter SL2, B: The Terrameter SL 2 and a car battery as external power source, C: Sensors are brought invasively into a borehole at different depths, D: The Teros 12 (METER Group, Inc. USA) sensor, it is equipped with one thermistor, the VWC is measured between the outer most needles and the EC is measured between the upper and middle needle.

resistivity values. A maximum tolerance of 5% was established for the staking error. Afterwards, a triangular mesh – accounting for complexity and flexibility in topography – was then constructed as reference for the inversion. A regularized solution with a linear filter (model misfit term) was implemented. The relative error in magnitudes was approximated to be 2%, while the minimum magnitude error was set to 1%. For each

iteration, the greatest misfit reduction was selected. The termination point was set to a maximum of 10 iterations or a final misfit of 1.0 as convergence threshold. In order to avoid the exclusion of any solution while remaining within the confines of reasonable physical possibility, the possible apparent resistivity range after inversion was set to a range of $(10^{-10} - 10^{10}) \Omega \cdot m$. In case where any normalized error exceeded an absolute value of 3 after inversion, the inversion calculations were repeated, excluding this data point.

4 Experimental Results

4.1 Overall ERT and sensor data processing

This section exemplifies the processing for an ERT, based on the measurement on August 28th 2024 at study site 2. Around that time the thaw depth reached this years maximum, which occurs usually around August and September. Furthermore, mainly the sensor data of one borehole (S 2.1) is processed and discussed. This implies that all subsequent analysis can be generalized, summarized and consolidated. Perspectives are presented and discussed in the Ch. 6. All obtained ERT are summarized in App. A.

4.1.1 Basic ERT

The resulting filtered and inverted ERT is shown in Fig. 5. The ERT is characterized by homogeneous stratification with increasing electrical resistivity at depth. Two spots of higher electrical resistivity lay at around 20 m and 60 m distance from the top.

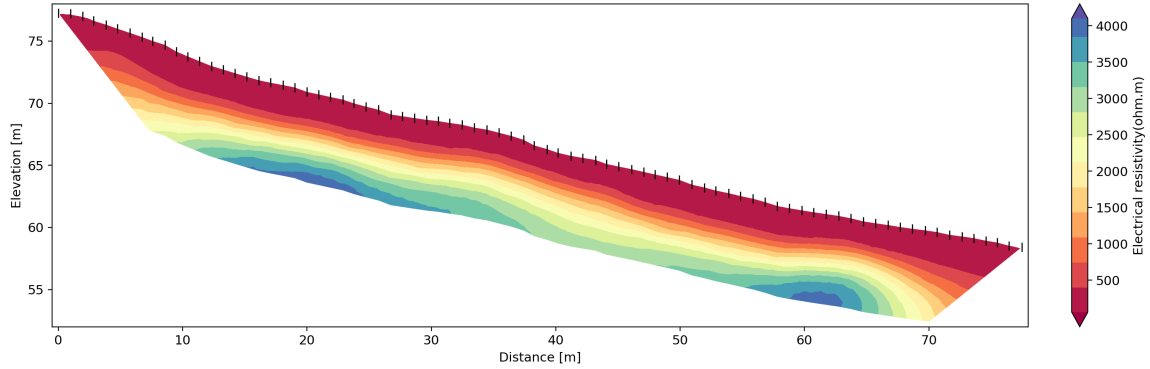


Figure 5: ERT at study site 2 on August 28th 2024. The rod electrodes are displayed as vertical lines which reach 10 cm into the ground. The figure was created using ResIPy [47].

The layering can also be presented numerically: In Tab. B.5 for every meter in depth the electrical resistivity means are shown. The means increase monotonously with the depth from $(135 \pm 33) \Omega \cdot m$ for the upper most meter to $(3340 \pm 490) \Omega \cdot m$ for a depth of 6-7.36 m. Except in the first two meters, the relative error decreases with depth, between one to three meters the relative error seems to be stable around 40%.

In App. B, Tab. B.6 different dynamic height ranges were calculated, all of which should be at least 5 cm great and further have a relative error of about 20%. Two regions from 7 m to 4.6 m and 1.2 m to 0.3 m could be identified as significantly homogeneous.

The sensors, which were used for analysis, were the ones within location ID S 2.1 (see also Tab. 1 for further information). A virtual borehole – an electrical resistivity column – was calculated for the ERT at the most proximate distance and at the same height as the sensors (Fig. 6). Furthermore, the mean value for a $30 \times 30 \text{ cm}^2$ area around each sensor position in the ERT was calculated and compared to the sensors (deviation) in Tab. 4.

Table 4: The electrical resistivity was calculated for a $30 \times 30 \text{ cm}^2$ area at the most proximate distance from the ERT line and the sensors and at the same height as the sensors.

Depth (cm)	Deviation($\Omega \cdot m$)	Combined error ($\Omega \cdot m$)	Deviation (σ)
10	1002.50	1290.13	0.78
50	478.78	375.45	1.28
100	133.00	79.35	1.68
150	211.33	24.74	8.54
190	121.45	242.29	0.50

The combined error includes both the standard deviation of the mean ERT values and the sensor error. The deviation between the mean ERT values and the sensor measurements is less than two σ except for 1.5 m depth. The deviation decreases by depth except at 1.9 m.

4.1.2 Permafrost estimation

The concept of the virtual borehole allows for the calibration of the ERT using the installed temperature sensors, assuming that the subsurface structure is homogeneous. If the geological structure is similar for all depths, the thaw depth becomes very clear as there is a steep increase in electrical resistivity. The use of surrounding temperature data enhances the accuracy of the layer transition even further and serves as calibration. The sensor data is linearly interpolated to find the depth at which the temperature is zero degrees. Due to the high temperature variability of the uppermost points (10 cm, 50 cm),

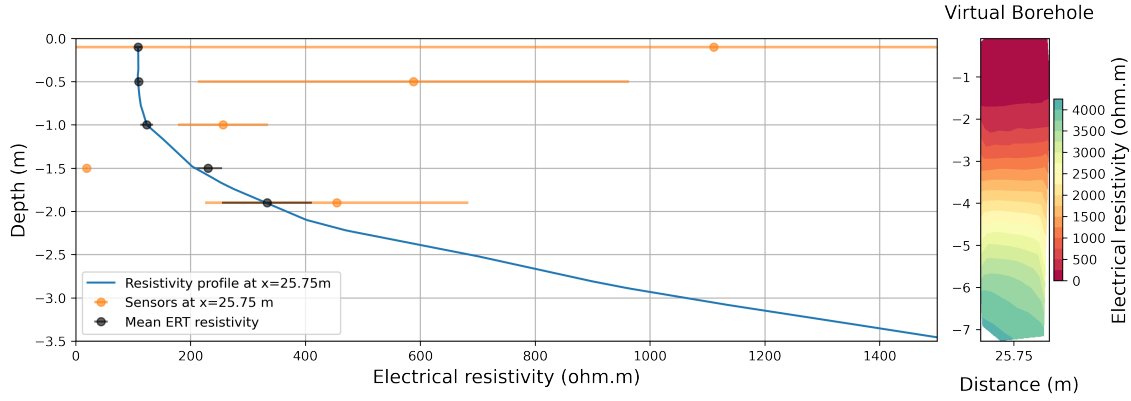


Figure 6: Left: The electrical resistivity profile obtained from the ERT line close to the sensors S 2.1 with the means of the surrounding $30 \times 30 \text{ cm}^2$ area and sensor measurements; Right: The virtual borehole showing the electrical resistivity profile.

these are excluded from the interpolation, as they are exposed to weather data and fluctuations rather than climate (see also Fig. B.3). The depth at which the temperature reaches 0°C is $D_{21}(T = 0^\circ\text{C}) = (-1.82 \pm 0.65) \text{ m}$ for study site and sensors S 2.1. For the sensors S 2.2 $D_{22}(T = 0^\circ\text{C}) = (-1.48 \pm 0.07) \text{ m}$. D_{21} corresponds to an electrical resistivity value of $(316 + 157 - 385) \Omega \cdot \text{m}$ and D_{22} to $(357 \pm 35) \Omega \cdot \text{m}$.

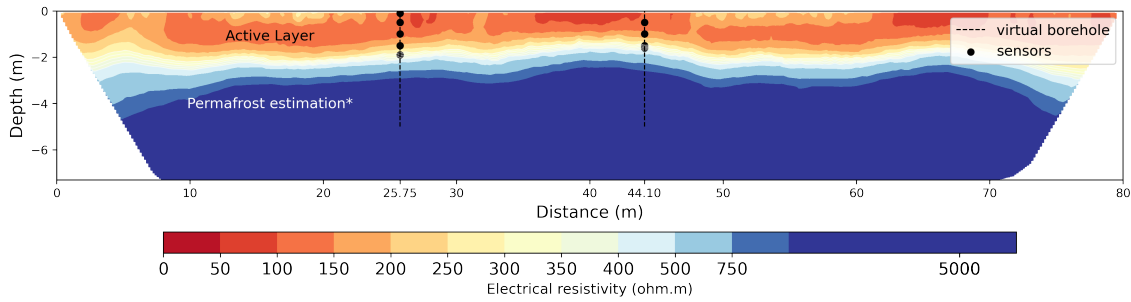


Figure 7: The permafrost estimation based on temperature sensors and the ERT.

Fig. 7 is divided in a dark blue area indicating permafrost overlaid by a white transient layer and the active layer. The transient layer reaches from $300 \Omega \cdot \text{m}$ to $375 \Omega \cdot \text{m}$. In the Fig. it is assumed that the thaw depth ($D(T = 0^\circ\text{C})$) also represents the border between permafrost and the active layer. This assertion is supported by the observation

that, around that time, the overall temperatures for all depths were the highest recorded for this year (see also Fig. 8).

4.1.3 Sensor data

In the following Figs. [8, 9, 10] the temperature, VWC and ER trends are shown. Generally the temperature at 10 cm depth is the most variable. Temperature fluctuations decrease by depth. The sensor errors become significant for deeper depths as the values are low but its errors remain high at ± 0.5 °C for values greater than zero and ± 0.3 °C otherwise. For the different depths, the VWC values are heterogeneous (Fig. 9). There are a few prominent peaks, especially in early June 2024 for all depths simultaneously, additionally at 100 cm in mid-July and from mid-August 150 cm is constantly at a very high magnitude ($0.40 \text{ cm}^3 \text{ cm}^{-3}$) and only decreases end-September. The peaks at 10 cm depth and at 50 cm are smaller but more frequent than for other depths. The VWC at 190 cm is generally the most constant, varying only between $0.12\text{-}0.16 \text{ cm}^3 \text{ cm}^{-3}$ within the measurement period. For 50 cm there are only two medium peaks in early and mid August. Apart from the significant peaks at 100 cm, the VWC curve is also relatively stable. Starting in October, all curves decrease.

The EC and ER data from all sensors have disproportionate high errors. The conductivity is generally low, staying below $50 \frac{\mu\text{S}}{\text{cm}}$ most times for all depths except 150 cm. For these depths from the beginning of August on the EC is as high as $200\text{-}600 \frac{\mu\text{S}}{\text{cm}}$ at an elevated constant level. For 100 cm two larger peaks reaching $75\text{-}150 \frac{\mu\text{S}}{\text{cm}}$ are visible. The freezing and a resulting decrease of VWC, EC and temperature is recognized in early October. The error ranges of most depths overlap each other. This makes the results difficult to analyze and interpret.

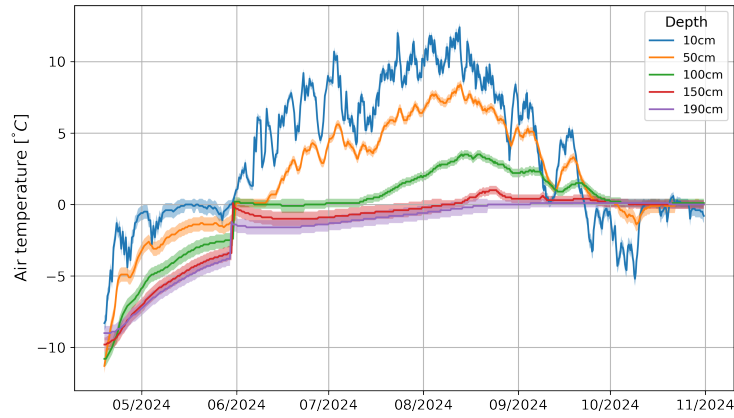


Figure 8: Long-term temperatures recorded by the sensors S 2.1 at depths reaching from 10 cm to 190 cm.

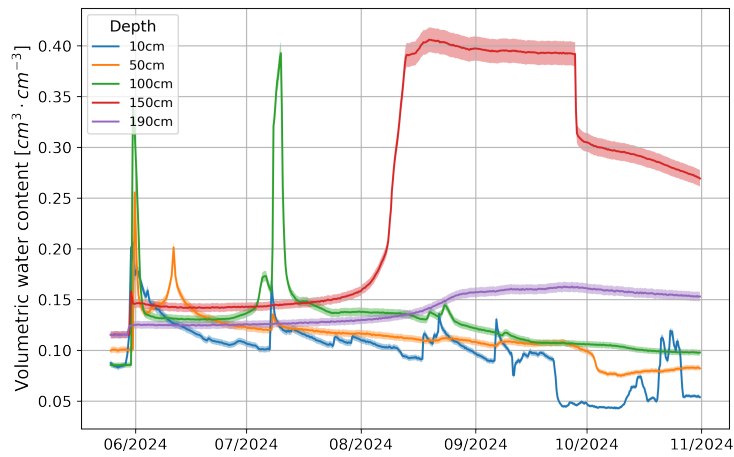


Figure 9: Long-term VWC recorded by the sensors S 2.1 at depths reaching from 10 cm to 190 cm.

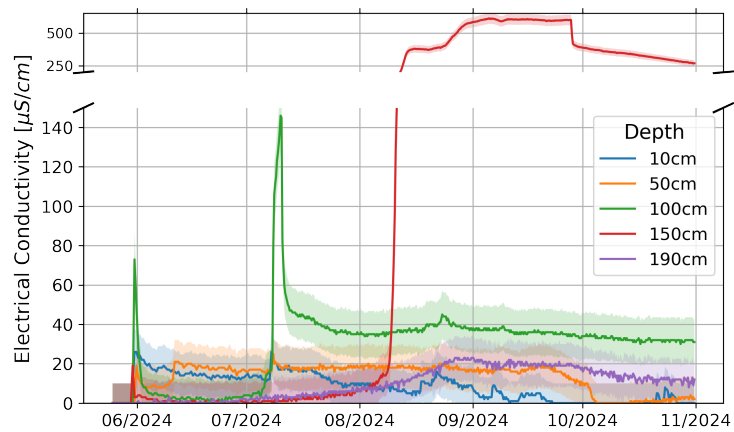


Figure 10: Long-term electrical conductivity recorded by the sensors S 2.1 at depths reaching from 10 cm to 190 cm.

4.2 Finding the best correlation between electrical resistivity (ER) and volumetric water content (VWC)

4.2.1 Random forest estimation

To quantify the correlation between ER and VWC, a machine learning model based on the random forest concept was used. For all models, 100 decision trees were trained with 80% of the input data and evaluated for the complement 20%. As a split quality measure the mean squared error was minimized at each node. All data were recorded in the period from 18 June 2024 to 31 October 2024 by the sensors S 2.1. The error of VWC was chosen as the weights for all such models. For model one (Fig. 11) only ER and its error were selected as features. Separate models were created for all depths.

In the following Figs. (11, 12, 13, 14, C.7) the shaded area depicts the VWC measurement $\pm 3\%$. The lines indicate the VWC value predicted by processing the ER sensor data point. Generally, the VWC trends were met by the predictions, lacking in details for some time points. The mean absolute error (MAE) ($\frac{1}{n} \sum_{i=1}^n |y_i - \hat{y}_i|$) is below $0.01 \text{ cm}^3 \text{ cm}^{-3}$ for all depths while the maximum relative error (MaRE) ($\max \left(\frac{|y_i - \hat{y}_i|}{y_i} \right)$) varies between 14% to -52%. The mean relative error (MRE) ($\frac{1}{n} \sum_{i=1}^n \frac{|y_i - \hat{y}_i|}{y_i}$) is below 10% for all depths ranging between 2.3% to 6%.

A more sophisticated approach used in model two, includes air temperature and precipitation (Fig. 12). Weather data were available at 10 min intervals from the Longyear dalen Central Station (SN99857) of the Norwegian Centre for Climate Services. As ER and VWC were only measured every six hours (3:30, 9:30, 15:30, 21:30), the temperature measurements for every 6 hours between two measurements were averaged and related to the later value, the precipitation was accumulated.

Adding weather data decreased the MAE and MaRE significantly for every depth. The reduction in MAE to below $0.005 \text{ cm}^3 \text{ cm}^{-3}$ for all depths is particularly evident. This is equivalent to a decrease of the MAE of 7.3% and 10.7% for 10 cm and 50 cm and 43.0% for 100 cm and even close to 70% to 75% for 150 cm and 190 cm. The MaRE for 100 cm remains relatively high at 51.4%. Nevertheless, the predictions are mainly in the $\pm 3\%$ range of the VWC measurements, with a few exceptions. This is also shown by MRE values between 0.7 and 3.7%. For 10 cm from late September until mid October there were no data because EC reached zero and these were excluded.

As the influence of air temperature and especially precipitation is assumed to be delayed differently for each depth due to an infiltration effect, a depth-dependent delay has been introduced. The delay was constraint between 0-72 h before the measurement to reduce coincidental minima which could result in overfitting the training data and reducing the prediction accuracy. In addition to temperature and precipitation, ER was also varied and delayed to enable potential forecasting. A summary of all delay times and associated errors is presented in the Tab. C.8. The errors can also be displayed as a function of the three delay times in a three-dimensional plot (App. C). The cube can be reduced in size by limiting the potential delay time from 0-72 h to 24-72 h, 36-72 h, and so forth, which may be applicable to forecasts of the VWC. The MAE minimizing delay times for all depths are summarized in Tab. C.8 and Fig. 13. The optimal results are obtained, when the temperature is incorporated into the estimation with immediate responsiveness, extending to a depth of 100 cm. For greater depths, the preferred temperature delay increases to 30 h and 36 h between the depth of 150 cm to 190 cm, respectively. The precipitation delay for shallow depths is initially significantly delayed (60 h), but then decreases with increasing depth to 12 h.

The optimal estimation of VWC uses the current ER measurements and combines this with depth-dependent delayed air temperatures and precipitation in Tab. C.9. The ER delay was left zero despite there being similarly small errors for delays reaching up to 66 h (combined with other delay times for precipitation and temperature than Tab. C.9). Nonetheless, these minima were neglected. Introducing these delays reduced MAE further by 16.8% to 33.8%. The MRE could also be reduced for all depths and 2.8% were never exceeded. The MaRE also decreased below 20% for all depths.

The best delay times for available parameters from 24-72 h are calculated and shown in Tab. C.10. The temperature dependence for the 24 h forecast demonstrates a gradual elevation with depth between the 24 h and 66 h. Conversely, the delay for precipitation exhibits considerable variability across all depths. A comparable trend is observed in the optimal delay of the ER measurements. In contrast to precipitation, a longer delay is identified as optimal for greater depths, with the variations being less pronounced (see table C.10).

The MAE increased and so did the MaRE. For 50 cm both MAE and MaRE stayed similar while for 190 cm both errors decreased even further. The MaRE increased significantly for 10 and 100 cm. Both, the best estimation and 24 h forecast remain mostly in the

± 3 % range of the VWC measurements, as quantitatively supported by the MRE, which stays well below 3% except for 10 cm. There, it slightly increases from 2.52% to 4.31%. Nonetheless, some inaccuracies are visible for the 24 h predictions. This becomes more prominent for 36 h forecast models and 48 h forecasts (Fig. C.7). The MAE and MaRE increase partially significant.

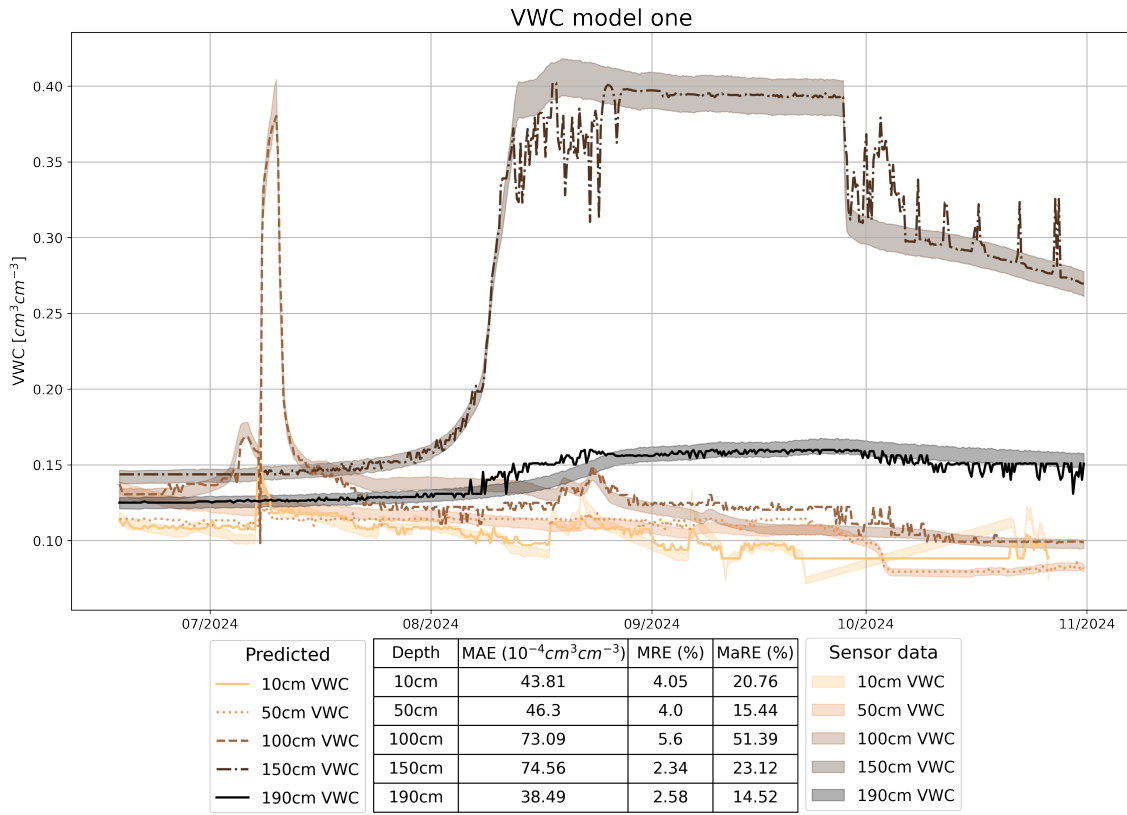


Figure 11: Naive random forest approach correlating ER and VWC; MAE is mean absolute error and MRE is mean relative error.

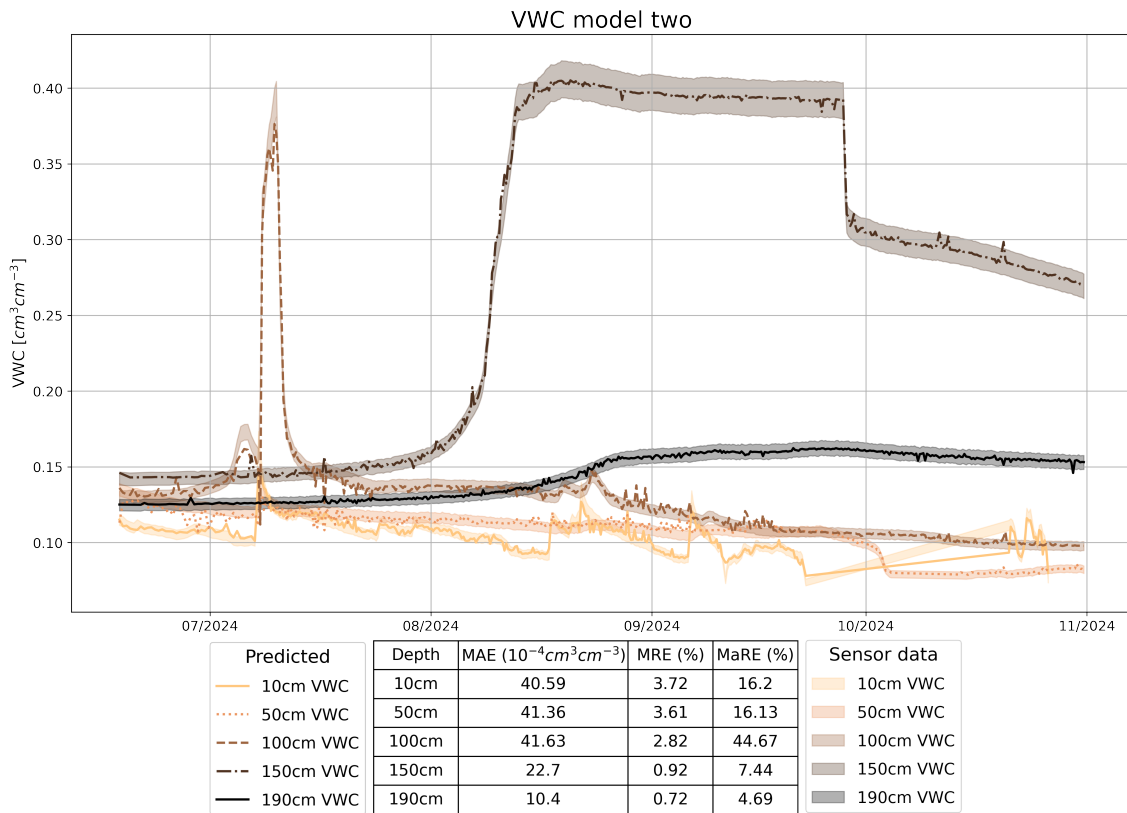


Figure 12: Random forest approach correlating ER and VWC including air temperature and precipitation data.

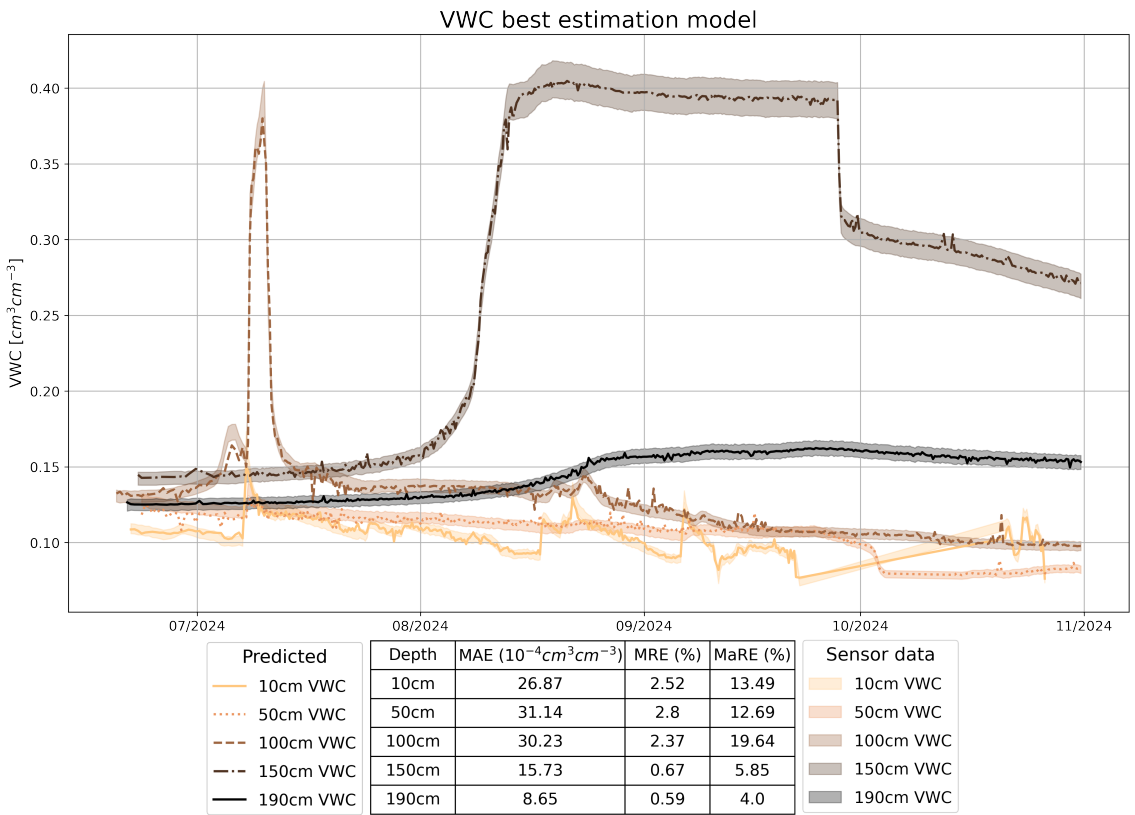


Figure 13: Model of best VWC estimation.

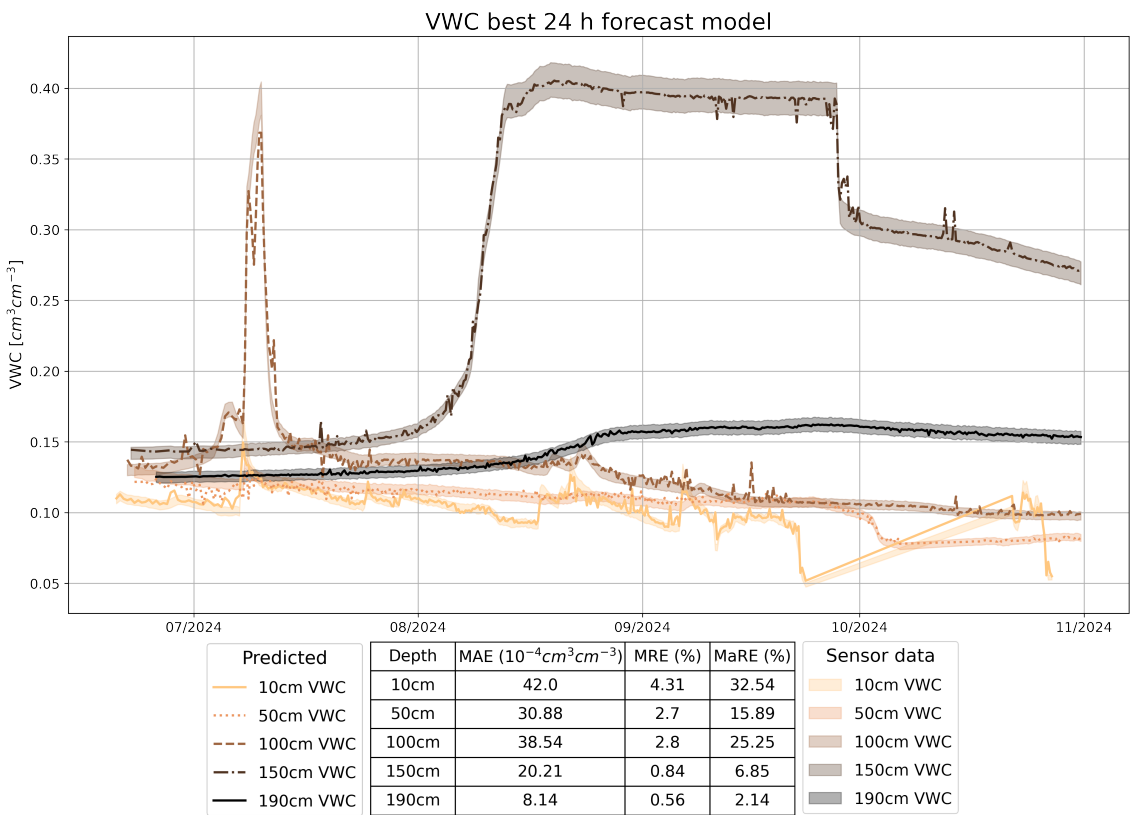


Figure 14: Model of best 24 h VWC forecast.

4.2.2 VWC estimation and forecast from ERT

Up until this point, a distinct model has been developed for each depth, with unique delay times yielding the lowest possible error. To extend the predictions to the entire ERT area and to obtain a tomographic reconstruction of the VWC estimation based on the ER measurement, it is necessary to interpolate the delay times for each depth. In the case of temperature and precipitation, the delays can be divided into 10 min intervals, as this is the smallest measured interval. For the best estimation, ER was taken into consideration without any delay, while for the forecast, ER was delayed by at least 24 h. Since ER is measured by the sensors every 6 h, the depth intervals are therefore generated summarizing every 6 h delays as indicated by the shaded regions in right Fig. 15.

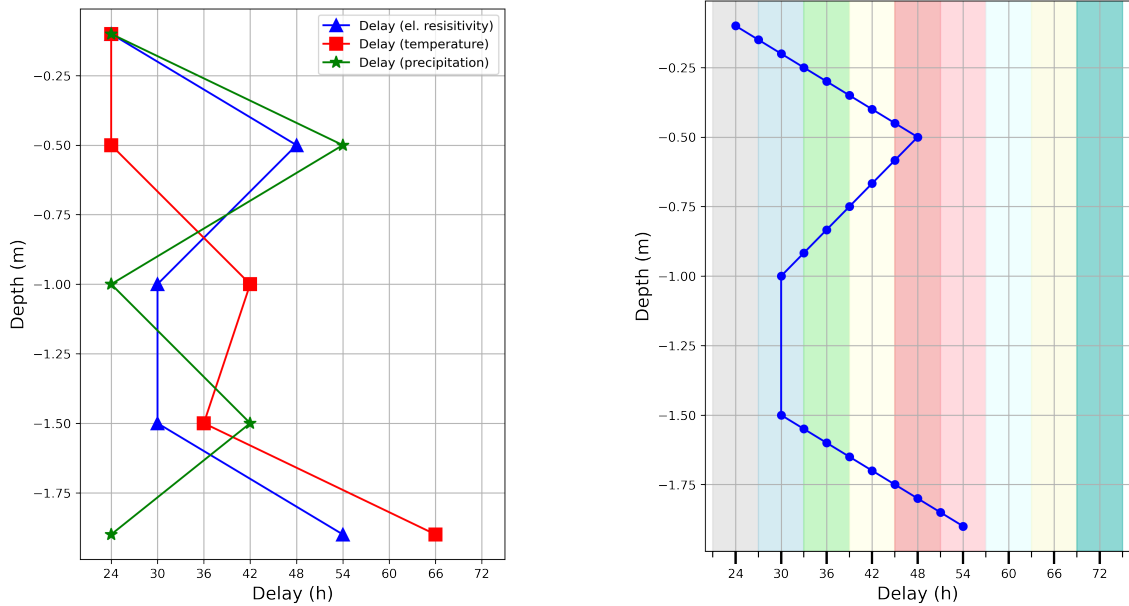


Figure 15: Left: Interpolated 24 h forecast delays for all features depending on depth. Right: Interpolated 24 h forecast delays for ER measurements and shaded 6 h delay intervals.

The interpolated delays and the different models for all depths can now be applied to both the ERT and the sensor ER measurements. Additionally, predictions were made with delays in accordance with the 24 h forecast. In the evaluation of the ERT values, only the most accurate estimation was used, given that no subsequent ERT were recorded at prior 6 h intervals.

It can be observed that both the predictions based on the ER sensor data and their best estimation agree well with the VWC measurements. The deviations between the VWC sensor measurements and the ER sensor VWC estimations are scattered below 0.6σ and except for the 10 cm and 100 cm data also below 0.2σ . For the VWC predictions from the sensors, only 10 cm and 50 cm exhibited larger deviations with just under 1.5σ while the other depths deviated only minimally ($< 1.0 \sigma$). Contrary, the discrepancies between the optimal estimation and the prediction from the ERT are evident, with the former exhibiting a narrower range of error (below 8.2σ), while the latter displays a somewhat broader range (between 0.2σ and 39σ) (see also Tab. C.11). Nevertheless, in comparison to the sensor estimation and prediction, the error margins associated with the ERT estimations and predictions are significantly more pronounced. Furthermore, it is evident that the predicted VWC of the ERT is in some instances significantly divergent from the measured values. The occurrence of discontinuities can be attributed to the use of a specific depth model in each of the shaded boundaries. Nevertheless, the VWC for the entirety ERT area can be estimated in Fig. 17. It can be reasonably presumed that the discrepancies between the predicted and actual values are likely to be as significant in other areas as they are for the virtual borehole. Nonetheless, a moisture zone can be identified at depths between one and two meters, exhibiting relatively constant characteristics across the entire ERT line.

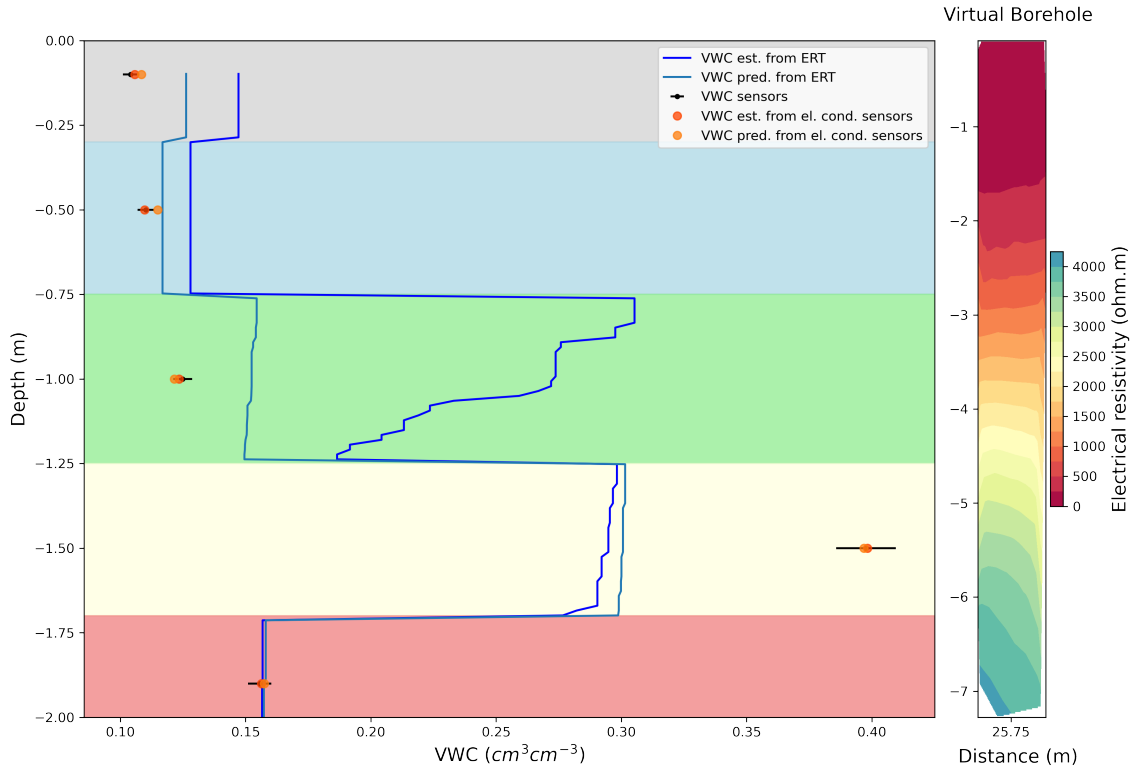


Figure 16: Left: Comparison of the VWC sensors, ER sensor estimated and predicted VWC and ERT estimated and predicted VWC.

The best VWC estimation of site 2 on September 04th. 2024 is shown in Fig. 17.

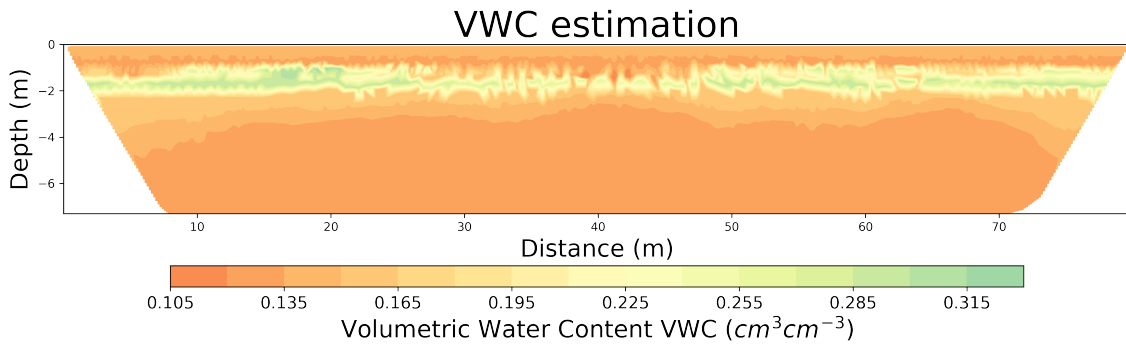


Figure 17: VWC estimation across the whole ERT area.

4.3 Survey one: short-term temporal variations

The objective of this survey was to assess the efficacy of the models in response to fluctuations or short-term changes in temperature and precipitation. Two measurement series were conducted, the first without significant changes in precipitation and air temperature and a second one including heavy rainfall.

The total precipitation of the first series of measurements was 0.7 mm at an average temperature of 2 to just under 13 °C as shown in Fig. D.8. The change in ERT is between -0.5% $\log \Omega \cdot m$ and 0.7% $\log \Omega \cdot m$ and is limited to small scale anomalies (see also Fig. D.10). The ER means do not change significantly (Fig. D.9). As expected, the VWC also changes little, with a maximum change of -0.15% $\log cm^3 cm^{-3}$ to 0.35% $\log cm^3 cm^{-3}$ (Fig. D.11).

For the second period, a control measurement was conducted 44 h before a large precipitation event. About 1 mm of rain fell between the control measurement and the heavy rainfall, the remaining 8.2 mm fell immediately before and during the first measurement. The average temperature was limited to 4.5-11 °C. In contrast, the first period, there was a larger change of -0.7-0.6% $\log \Omega \cdot m$ of the ER, but only locally limited, as can be seen from the constancy of the mean values (Fig. s D.13 and D.14). The means remained almost unchanged for all depths. At 10 cm the ER increased by about 15 $\Omega \cdot m$ in the last measurement. The resulting VWC estimates were also constant. Depending on the depth, the used delays of the precipitation data are as shown above (Tab. C.9) between 24 h and 66 h, which cancels the influence of the rain shower on the estimation of the VWC so close after the rain.

4.4 Survey two: spatial overview and validation

The second survey was conducted with the objective of transferring the results obtained for location 2 to the other research areas. The ERT and sensor measurements were performed at all sites in accordance with the methodology employed at site 2.

In order to create a unified representation of the recorded ERT, the sensor temperature data was processed to identify the depth at which the temperature reached 0 °C. This value was then marked as a white line in Fig. 21 (at the end of the section). The deepest thawing was observed at study site 3 at $D_{S31}(T = 0^\circ C) = (-2.037 \pm 0.005) m$ whereas ID 4 and 5 lied at $D_{S4}(T = 0^\circ C) = (-1.900 \pm 0.005) m$ and $D_{S5}(T = 0^\circ C) = (-1.958 \pm 0.015) m$.

The shallowest depths, nearly 40 cm above D_{S31} were the areas 1 and 6 with $D_{S11}(T = 0^\circ\text{C}) = (-1.61 \pm 0.21) \text{ m}$ and $D_{S6}(T = 0^\circ\text{C}) = (-1.634 \pm 0.003) \text{ m}$. The sensors S 1.21 and 1.22 were not installed at that time. The ER at these depths ranged from just below $200 \Omega \cdot \text{m}$ at ID 3 to nearly $500 \Omega \cdot \text{m}$ at ID 5. Precipitation between the measurements accumulated to 2.40 mm and the air temperature was stable between the measurements. Differences due to meteorological influences were minimized (see Fig. E.15).

Significant variations in ER values between different locations were observed. Generally, study sites 1 and 3 show low ER values, followed by ID 2 and 4 whereas 5 and 6 exhibit very high ER.

Where available (S 3.12 and S 3.2), the estimated and predicted VWC based on the models trained with measurements from site 2 was tested against the sensors of another site. A comparison of Fig. 18 with Fig. 10 and Fig. 9 shows that the EC and VWC ranges of the two sites differ significantly. Corresponding deviations for the VWC estimations become visible in Fig. 19.

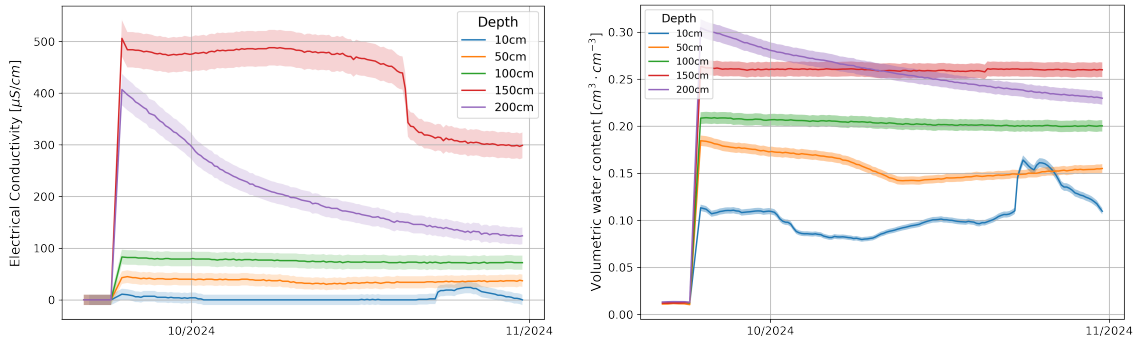


Figure 18: ER (left) and VWC (right) measurements for ID S 3.12.

The trained model for 190 cm was used to estimate the 200 cm sensor data. All evaluation metrics indicated a significant deviation between the estimated and measured values. This was also confirmed qualitatively. The estimates did not fit the measurements well at any point. The 10 cm and 100 cm estimates were the best, with an MRE of just under 12% and 8%. The estimates at other depths exhibited substantially higher absolute and relative errors. The estimates for ID S 3.2 and S 1.2 showed similar deviations. Reverse training with sensor data from ID S 3.12 also led to unsatisfactory results for estimates of ID S 2.1 values.

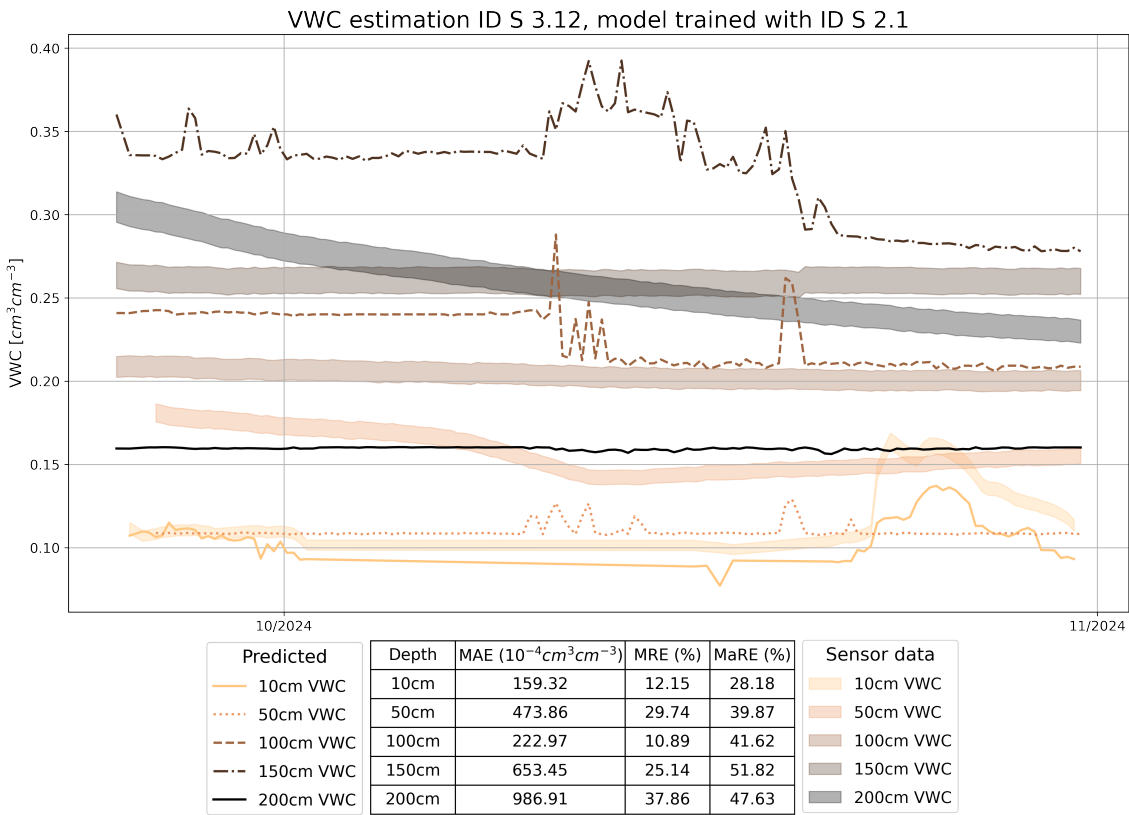


Figure 19: The trained RF models with ID S 2.1 data were applied to the sensor values for sensor ID S 3.12.

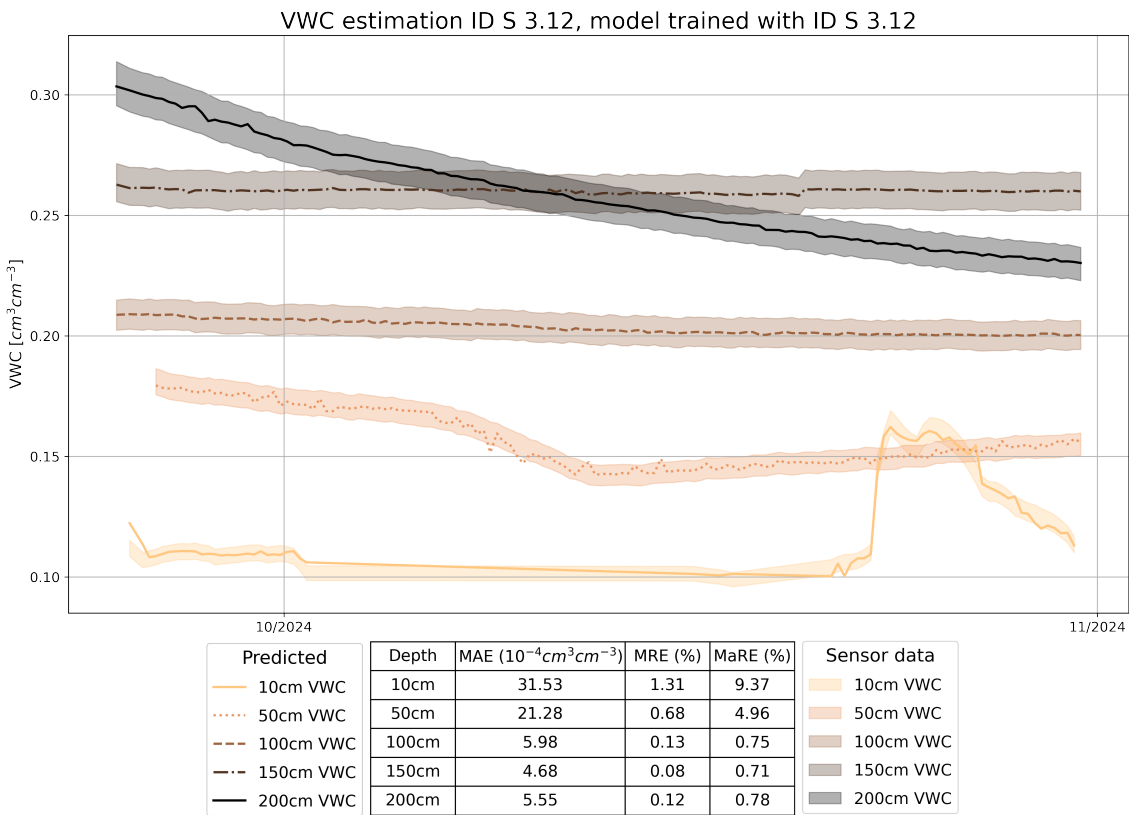


Figure 20: Separate RF models were trained based on ID S 3.12 data and tested with ID S 3.12.

However, if separate models are trained on the data from ID S 3.12, this data can also be visualized with high accuracy, resulting in minimal MAE and MRE (see Fig. 20). There are also no outliers (MaRE below 1% except 10 cm (1.3%)). The limited available time interval and meteorological variations may have been smaller as the ground was generally colder. The data were trained with the best delays from the best estimate for ID S 2.1.

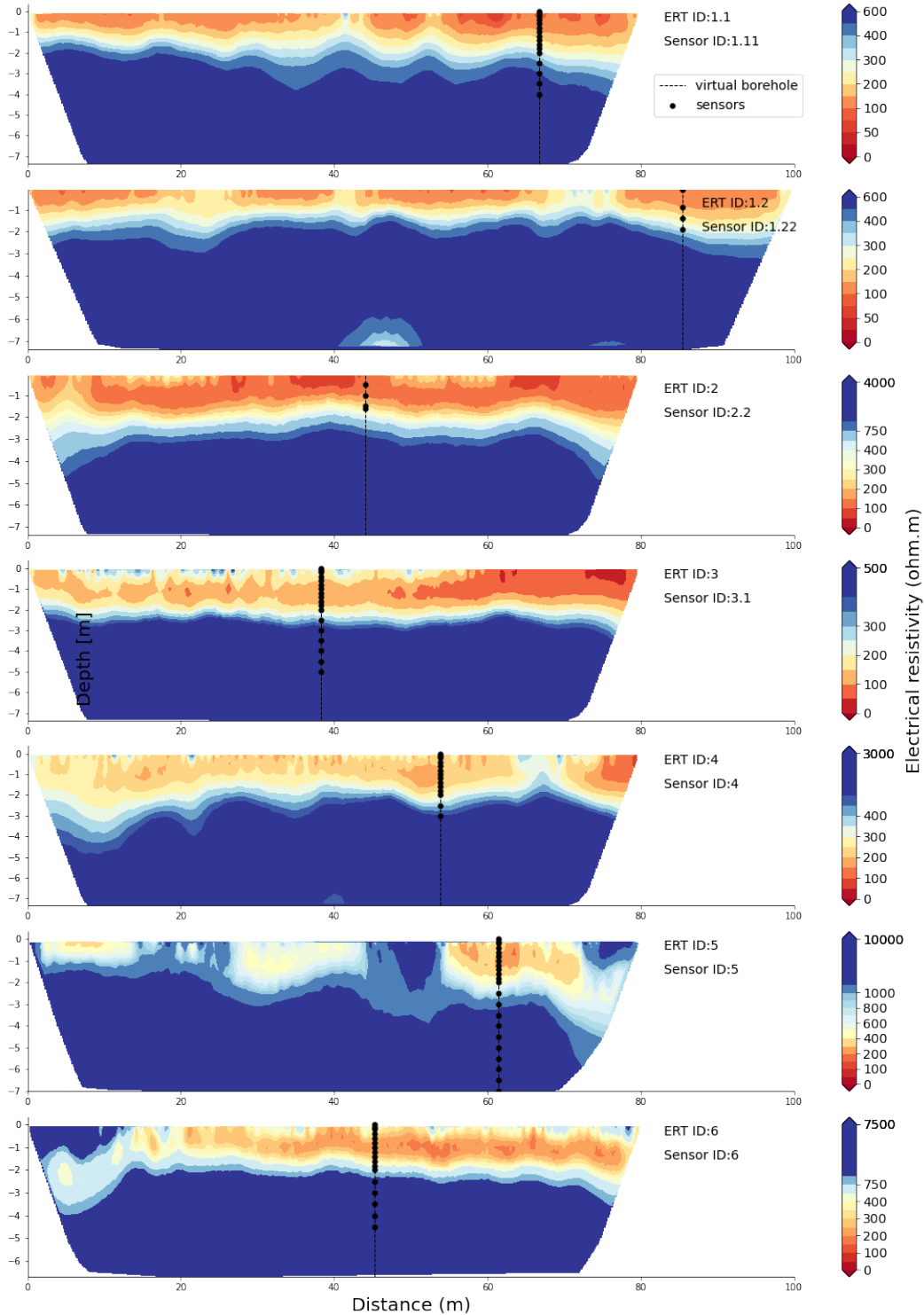


Figure 21: ERT from the different study sites across Longyearbyen, calibrated by their depth at 0 °C.

4.5 Survey three: temporal long-term temporal variations

The aim of this third survey is to investigate seasonal differences in the ER and, in particular, the transition from summer and the thawed active layer to the freezing of the entire ground. The $\% \log \Omega \cdot m$ differences are shown in Fig. 22 for the weekly measurements with the first ERT as reference.

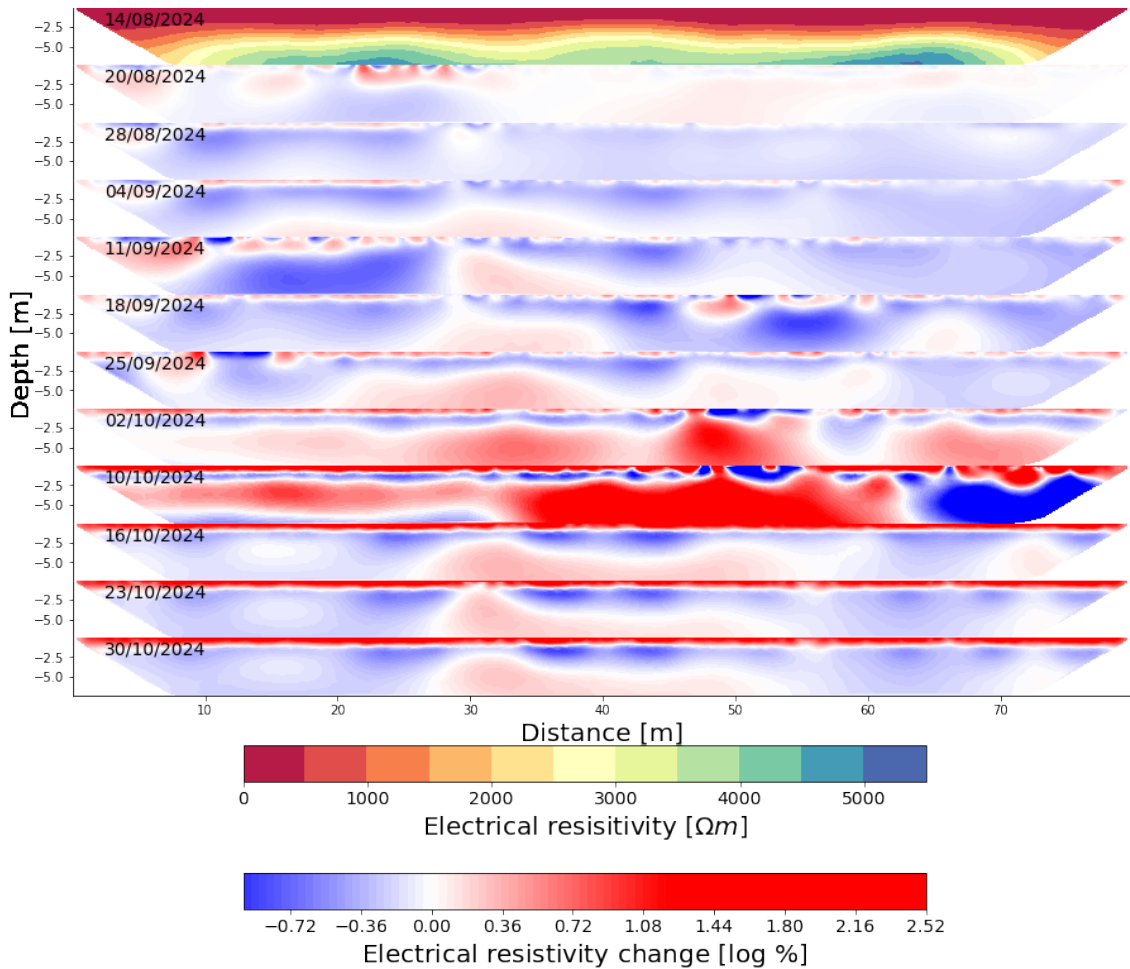


Figure 22: Seasonal long-term variations for study site 2.

Freezing becomes visible from the beginning of October. In the uppermost layer and in the permafrost, the ER increases strongly and reaches magnifications of 2-2.4 $\% \log \Omega \cdot m$. The ER in the permafrost also increases mostly, except for distances from 65 m to 80 m. A small layer for which the ER decreases, is evident at 1.5-2 m depths. There is still

water in a liquid state (see also Fig. 9). In the following week (16.10.2024), the air temperature increased again, whereupon the ER decreased again. The topmost layer was still frozen and stayed frozen until the measurement period end. The overall ER stayed in the following weeks relatively constant.

Complete freezing was not recorded, as the measurements had to be canceled at the beginning of November after the risk of avalanches increased due to snowfall.

5 Discussion

In this work, sub-surface ER and VWC structures in Longyearbyen were investigated using electrical resistivity tomography. The ERT data was fitted to temperature data, the thaw depth and permafrost estimation were visualized. Next, the ERT was compared with the ER sensors.

A random forest model was trained using ER and meteorological data to predict VWC. To validate the general accuracy and robustness of the resulting model, different scenarios were selected and evaluated, representing temporal, meteorological and local variations. Finally, the seasonal change of permafrost from summer to winter was observed.

5.1 ERT monitoring

5.1.1 ERT acquisition

The active layer was not yet frozen at the beginning of August when the first measurements started and neither at the beginning of September when the other sites were measured. Therefore, it was relatively easy to insert the electrodes into the soil. However, in some places, particularly at sites 5 and 6, there were a lot of stones, which made it difficult to place the electrodes. This was also reflected in the higher contact resistance. Nevertheless, all ERT could be carried out as planned. Straight ERT lines could be measured with 101 and 81 electrodes respectively for study site 1.2 and the others. It was not always feasible to maintain a strict spacing of one meter from neighboring electrodes, as is evident from the GPS data. Height data acquisition with the Leica GNSS 16 device was not successful, the measured height differences between adjacent electrodes were sometimes obviously higher than in reality. A satisfactory explanation for this has not yet been found. Instead, heights were determined using GPS data and a DEM model with a 2.5 m resolution. There were also some large differences between adjacent electrodes due to the resolution of the DEM, which had to be interpolated. This involved averaging 3 adjacent electrode heights. This inevitably leads to a linearisation of the DEM line, which is only an averaged representation of reality.

The filtering of the data was successful without major limitations, the eliminated data was always less than 5-10% of the total data. The criteria defined for sorting out the erroneous data followed the conventions of current research [8, 9]. The data inversion was carried

out with a least-squared data misfit norm instead of an L1 because it was not implemented yet in the current ResIPy version (3.3.5). Although an L1 norm is advantageous for characterizing the boundary between the active layer and permafrost, however, since the focus for the VWC estimates lied on the active layer, these possible uncertainties are insignificant.

5.1.2 Characterizing ERT and permafrost soil estimation

The presented ERT data appear homogeneous, both qualitatively and quantitatively. The maximum relative error for the meter by meter depth subdivision of the ERT was 40%, with deviations between 15% and 25% calculated for over 50% of the total depth. This is relatively low compared to ERT in other areas [7, 9, 48].

The comparison of the sensor measurement with the ERT showed no significant deviations, except for the measurement at 150 cm. The insignificant deviations result from the large combined errors, which in turn are largely determined by the errors of the sensors. According to the manufacturer, the EC accuracy is $\pm(5\% + 0.01dS/m)$ from 0-10 dS/m and $\pm 8\%$ for values between 10-20 dS/m. For very low values (about 5-50 $\mu S/cm$), as measured at each site, the error is in the range of 10% to 150% of the measurement. In this context, it seems reasonable to assume that the actual deviations for all depths are as high as the ones for 150 cm. The root-mean-squared error (RMSE) of the ERT for all measurements is around 1.0.

The depths $D_{S21}(T = 0^\circ C) = (-1.82 \pm 0.65) m$ and $D_{S22}(T = 0^\circ C) = (-1.48 \pm 0.07) m$ have been determined as temperature zero depths from the temperature sensor data at study site 2. These are accurate for 28 August 2024 as they are continuously influenced by meteorological conditions. The error of D_1 is relatively high at 35.9%, which is due to the fact that only three sensors are placed in the relevant area, one of which, at $2.5^\circ C$, was already far away from $D(T = 0)$. It is possible that a linear fit was applied to the exponential part of the permafrost temperature curve. An adjustment would require an exponential fit to the given data or a further discrimination of the upper sensor, which in turn would lead to a higher uncertainty as only two sensor measurements would be available for estimation.

As the average temperature decreased in the following period, it can also be assumed that the measured thaw depth also represents the thickness of the permafrost. The assumption includes, that the thaw depth was not deeper last year. The depths correspond to the

surrounding measured annual maxima of the active layer [39]. Herring et al. [49] argued for an improved interpretation of ERT with temperature correction, however, it was highlighted that there is still much research to be done in this field, especially concerning partially frozen ground. That is why the data were not temperature corrected, one should be aware of interpretation.

5.1.3 Sensor data

The seasonal temperature variations decrease with depth, which is expected, as shallower depths are more influenced by seasonal and daily air temperature variations than greater depths (compare Fig. 8). There is a sharp rise in temperature at the end of May 2024 for all depths. The hypothesis is, that when the topmost layers thaws, the water penetrates along the sensor cable into deeper layers and washes around the sensors. Since the water has just thawed, it has a temperature of around 0 °C. This is supported by the observation that the sudden rise occurs when 10 cm is at 0 °C. Moreover, the VWC at all depths increases drastically simultaneously (Fig. 9).

The VWC measurements are also relatively accurate with a $\pm 3\%$ deviation. The peaks at 10 cm are attributable to precipitation, while the peaks at greater depths are due to subsequent successive infiltration. A decrease as rapid as the increase in the VWC curve suggests that the water continues to infiltrate downwards. The constant high level for 150 cm from mid-August is probably due to the fact that the frozen part of the ground begins between 150 cm and 190 cm, so that deeper penetration of the water is no longer possible and the water remains trapped. The decrease in VWC in early September can be attributed to the freezing of the water, given the decreasing temperature trends during this period.

The EC sensor readings (see Fig. 10) are difficult to interpret due to large errors. The Teros 12 sensors are clearly not suitable for such poorly conductive soils, so this data should be used with caution. Therefore, the quantitative data, especially in the following sections, are only recognized as reasonable under these circumstances.

On 18 September 2024, an automated-ERT (A-ERT) system was installed next to the ERT ID 2 line, so that the EC sensors can be replaced by repeated ERT in the future. Successful commissioning of the A-ERT was achieved on 07 November 2024, after the field laptop arrived. A detailed description can be found in Ch. 6.

5.2 Estimating and predicting VWC from ER measurements

In the research field of hydrology, one current focus is the search for a relationship between ER and VWC [7, 50]. ERT offers a cost-effective, minimally invasive and real-time alternative to the locally very limited, invasive sensor measurements [7]. Common approaches to correlate ER and VWC include curve fits, which requires the use of additional rock physics models and sample data [9]. Moreover, this approach may be applicable only at the local level due to the specification of local parameters [51]. Two common curve fits include the Archie equation (equation 2.1) and the Waxman-Smiths equation. Both equations are based on empirical parameters and are only reliable for certain soil types [21]. Furthermore, ER is not only influenced by VWC but also and not limited to mineral composition, temperature, precipitation and microbial activity [51].

The combination of remote sensing and machine learning has previously facilitated significant advances in the estimation of near-surface soil moisture content from satellite imagery [52, 53]. However, the spatial and depth resolution is insufficient to provide added value for local applications.

A compromise between point sensor measurements and area-wide analyses on a kilometer scale is represented by ERT. The present research employs machine learning models to correlate ERT and VWC [50, 54]. In a study published in November 2024, Meng et al. [7] compared various machine learning models for estimating VWC based on ERT data. The results demonstrated that the RF model outperformed all other tested models, exhibiting the lowest RMSE, the highest R^2 , and the most robust performance in the validity check. The random selection of possible features for splitting on a node has been set to two for all models. This provides greater robustness and a further reduction in variance due to the additional randomness [35]. However, this is achieved at the potential compromise of further accuracy, as the best split parameter is not always included and thus the best split possible is not realized.

In this thesis a separate RF model was trained for each depth. This ensures a better visualization of the VWC depending on the height, while depth-dependent delays can be implemented separately. In addition, better output stability can be expected as the respective input spaces are more centered. However, a favorable advantage still needs to be validated. The training and testing data from 18. June 2024 to 31. October 2024 yielded 370 to 500 data points after excluding measurement times with recorded electrical conductivities of 0 S/m , as otherwise the electrical resistance would approach infinity.

Comparable models were trained and tested with 270 data points, with further data used for validation purposes [7]. The onset of the training data from 18 June 2024 was selected to ensure the inclusion of the entirety of the available data set, while simultaneously excluding any instances of inaccuracy pertaining to the thawing of the upper layer and the subsequent infiltration of water around the sensors, as previously described.

This thesis employs an extensive temporal validation with survey one and a comprehensive spatial validation with survey two. Three evaluation metrics were selected to quantify the prediction outcomes. The mean absolute error (MAE) was chosen as a measure of the overall predictive power, whereas the mean relative error (MRE) was chosen to represent the discrepancy between the predicted and actual values in relation to their magnitudes. In addition, the maximum relative error (MaRE) was considered as a further measure of outliers.

A detailed evaluation of the individual models revealed that on occasion the MaRE exhibits a notably elevated level. The model for 100 cm exhibited significant difficulties in consistently providing reliable predictions. This is particularly evident after the pronounced peak observed in mid-July. Furthermore, the MAE, MRE and MaRE values are also higher compared to those of other models. Additionally, substantial individual deviations (up to 52%) are apparent. This is likely attributable to the simplicity of the models, which only receive two inputs (ER and VWC) and are trained based on depth. Without this depth information, the models' performance is likely to be even more adversely affected, as demonstrated by Meng et al [7]. The 150 cm model also encountered difficulties in achieving a consistent estimate. However, the errors remain relatively low, due to the fact that only relatively short (in absolute terms) deviating peaks are present, and the total VWC is also increased in comparison to the other depths. This results in lower relative errors. From late September until mid October the VWC for 10 cm was affected by freezing. The models were programmed that data points with EC measurements of zero were excluded. One solution would include to set a relatively low value for the VWC in situations where the EC is zero. Nevertheless, in the cases of ground freezing, stability is enhanced, which makes the estimation of VWC values an arguably superfluous endeavor.

5.2.1 Influence of meteorological parameters

Since air temperature and precipitation have a major impact on ER and VWC, they were included in the second model [9, 55]. The meteorological data was taken from

Longyear dalen Central Station (SN99857) approximately 300 m from the study site 2. It is plausible that local disparities may have been introduced as a result. Nevertheless, a decrease across all metric values at each depth was observed. This allows for the hypothesis, that, provided that meteorological influencing factors remain relatively constant, there is no requirement to install an additional temperature and precipitation measuring station in immediate proximity to the ERT. Nonetheless, the installation of such a measuring station would yield even more accurate results. Including the additional features led to MRE values below 4% for all depths. Outliers have not yet been effectively filtered. These are primarily observed in instances of pronounced peaks in the VWC, which exhibit a high degree of correlation with the underlying trend. However, due to the pronounced gradients, the models are unable to provide precise quantitative values.

5.2.2 Influence of depth-dependent delays

The infiltration of precipitation can be calculated using a variety of equations, including Richard's and Horton's [56, 57]. The solution of these equations frequently necessitates the utilization of numerical techniques and the incorporation of empirically derived supplementary data. However, since precipitation has a significant influence on VWC [9, 56], a different approach was considered: The precipitation, air temperature and ER were delayed depth-dependent. For example, a cumulative precipitation of 4 mm over the previous 6 hours in the model at 50 cm is only assigned to the data point with the VWC measurement 12 hours later. In this method, precipitation, air temperature, and ER curves are processed accordingly. Prior to this, no modeling assumptions regarding an ideal depth-dependent delay were implemented. A delay range from 0-72 h was defined, as there is the possibility of random correlations arising for delays outside this range due to the size of the training data set. The combinations of delays for all three parameters were compared with one another (see Tab. C.8), and the MAE were calculated. In the following, two combinations of delays were further analyzed. The optimal estimation of the VWC was described with the parameters presented in Tab. C.9. The ER delay was adjusted from 66 h to 0 h for 50 cm and 190 cm, effectively disregarding the total ER delay. It seems probable that the two 66 h delays are the result of local minima. The optimal delay combination for both depths was calculated and resulted in only insignificantly higher MAE.

The introduction of delays resulted in a further reduction in the MAE. It is debatable

which of the metrics should be used for minimization. However, the MAE was deemed to be a clear measure of the accuracy of the model and therefore seemed appropriate. But it is also possible that minimization objectives could be set for RMSE or maximum relative error (MaRE), given that landslides are primarily caused by heavy rainfall, which results in a significant increase VWC in a short time period. To further analyze the correlation between the estimated and measured values for the best estimate, the root-mean-squared error (RMSE) and the coefficient of determination (R^2) for the best model were calculated and are shown in Fig. 8. The optimal monotonically continuous linear curve was found to fit for the majority of the data points, which are largely within the sensor uncertainty range of $\pm 3\%$ (shaded).

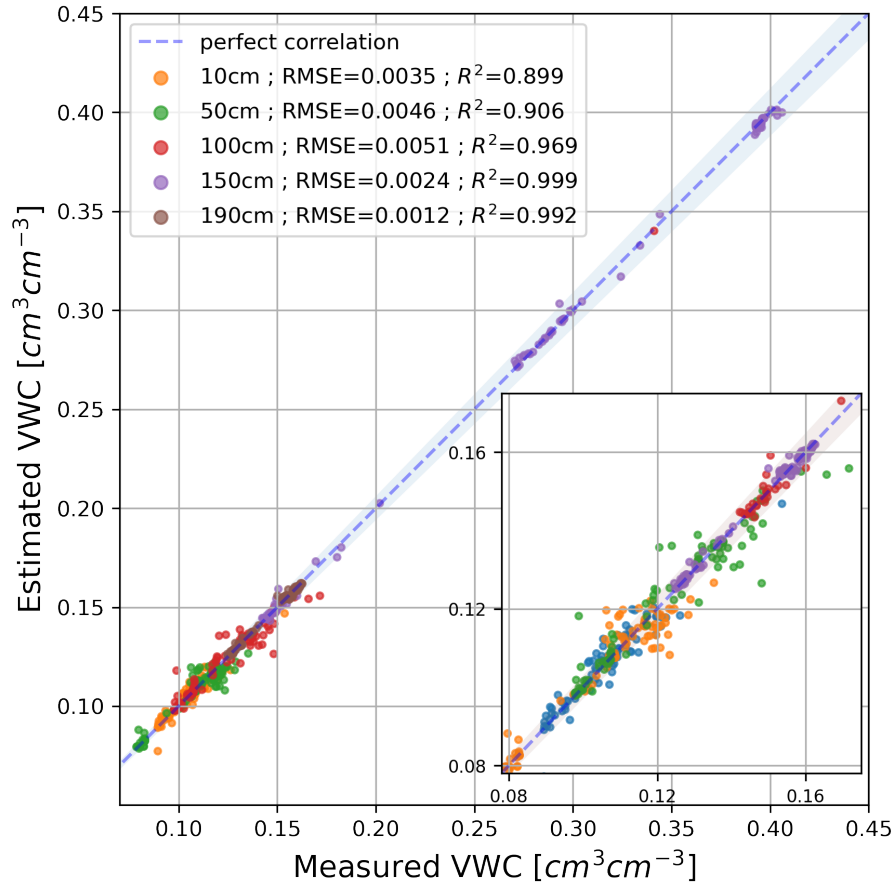


Figure 23: Estimated and measured VWC of the test data for the best estimation RF model.

Compared to literature sources [7, 9, 58], both the robustness and accuracy of all models are superior. The research conducted by Meng et al. [7] yielded R^2 values as high as 0.92 and RMSE of 0.0041 for their RF model. In comparison, the estimation proposed by Wicki and Hauck [9], based on Archie's Law, never exceeded 0.87 for R^2 . Their RMSE was as low as 0.004. Fu et al [58] derived separate values for different soil types by applying another petrophysical formula. The combination of all soils resulted in an RMSE of 0.041 and R^2 of 0.95 with ranging values for different soil types (RMSE: 0.020-0.051; R^2 : 0.91-0.99).

A 24 h as well as 36 h and 48 h prediction was selected based on the restriction of potential delay values to the intervals between 24 (36/48) and 72 hours. For the 24 h forecast small deviation became knowledgeable, especially for the MaRE. The choice to further investigate the 24 h forecast was a trade-off between temporal foresight and accuracy and robustness of the models. If desired one could vary minimization metrics and further forecast times.

5.2.3 Comparison of forecast to estimation

In implementing the depth-independent RF model, which was trained on sensor data, to the ERT data, the delays obtained for the five heights were interpolated in an effort to encompass the entire height spectrum of the ERT. For ER, temperature and precipitation, an increase in the delay with increasing depth was to be expected. The best estimated as well as the predicted best temperature delays were more or less depth-independent.

In contrast, the precipitation delays were higher, increased first but then scattered. The 24 h times did not agree the expectations. The forecast ER delays demonstrate an alternating pattern, initially exhibiting constant values and then increasing, before subsequently decreasing again after 100 cm. For all delays there was no recognizable pattern.

It is possible that no global minima but only local minima were reached and thus the delays do not increase with depth. Further discussion reveals that physical argumentation is not expedient. One approach to address this issue is to formulate assumptions in advance about the restriction of possible delays depending on their height. Upon applying the trained models to the aforementioned ERT and simultaneous sensor measurements, it becomes evident that, on the one hand, the estimates and predictions of the ER sensor measurements align closely with those of the VWC measurement. In contrast, the VWC predictions and estimates of the ERT do not agree well with the sensor measurements.

It is noteworthy that the ERT VWC exhibits a sudden change at the boundaries of the shaded regions. The aforementioned models were trained within these areas. Each region is represented by a distinct model. One potential solution to align these depth boundaries is to integrate all models and consider depth as a parameter, as proposed by Meng et al [7]. Nonetheless, it is mainly driven by the amount of depth VWC point available. Therefore, incorporating additional VWC measurement points would the depth variation more precisely. Furthermore, it is plausible that the ER training data of the models were not within the range of those employed for validation (ERT, domain shift). Consequently, a possible solution would be to train and test the models with ERT data as the ER measurement data sometimes differ greatly from those of the ERT, which was already shown in Fig. 6. A significant improvement can be expected when the A-ERT is put into operation and the ER sensors can be neglected. A shift of the training and test data from ER sensor data towards ERT data is expected to further improve VWC estimation from ERT similar to the current sensor data alignment. The fact that the prediction of the ERT measurement gives a better estimate of the VWC than the best estimate may be due to the way the RF models are constructed. For each node, the model decides on the optimal split parameter to minimize the error. In the forecast, ER may be chosen less frequently as split parameter. As previously explained, the best VWC estimate does not include a delay in the ER. However, the forecast includes a delay, hence VWC values for similar ER will be scattered, reducing the quality of the split.

Nevertheless, cautious estimation of the VWC can be conducted. A layer with a high VWC is apparent (Fig. 13), although it is likely to be overestimated in thickness (see Fig. 16). This layer extends from 75 cm to a depth of approximately 175 cm. The underlying permafrost is dry, as are the top few centimeters of the soil. It seems probable that precipitation infiltrate the upper layers of soil and then stagnates above the permafrost, since the ice establishes a natural boundary to the depth of infiltration.

5.3 Testing the RF model for short temporal changes

Since neither large temperature differences nor precipitation could have influenced VWC in the first measurement interval, any differences in VWC were due solely to differences in ER. No large differences were found either in the mean values or in the total ERT. Furthermore, the estimation of the VWC was apparently good throughout the period shown

in Fig. 13 and largely in the $\pm 3\%$ range for all depths. Not all 6 h ERT were carried out, which makes it difficult to check the predictive capabilities, as the delays of the ER would then always need to be rounded to the next possible ERT times. This could possibly deviate by up to 9 h from the actual delay value. For this reason, this approach was rejected as it would have introduced large uncertainties. Nevertheless, it can be assumed that the predictions have the same uncertainties as previous VWC estimates of ERT considering estimation and prediction capabilities for the sensors.

The heavy precipitation in the second interval did not lead to a significant change in the mean ER. This is probably because there are large but locally heterogeneous differences in ER. Since the regions of large increases and decreases in ER due to the depression are very close together, it is reasonable to assume that the water missing in one region is present in the other. It is possible that the water was able to penetrate the soil more easily. The VWC estimates and their changes are generally considered insignificant. Regarding the delay times previously obtained, it is plausible that the ERT was recorded too soon after the downstroke and that there is an error in the methodology. It is advisable to repeat the measurement of the influence of a large rainfall event with adjusted measurement times, taken further after the precipitation.

5.4 Testing the RF model at various different locations

The seemingly inappropriate estimates from all the other sites on the models from study site 2 are based on the fact that the ER and VWC values of the validation data fall outside the training ranges of the models (domain shift). As a result, they encounter ER values that they were not trained with, i.e. higher or lower than all the values they know, and then logically choose the highest or lowest VWC value that seems to fit best. Since all ER values are consequently higher than those for the study site, the same VWC value is always selected and a constant prediction is generated. This can be solved by providing additional data with a wider range of ER and VWC as training data. By increasing the available data it could be possible to make more accurate predictions. Therefore, it is useful to implement a study, in which all the test sites to be investigated (or at least the ones with the most extreme ER and VWC values in addition to some data in between) in one model.

Another source of uncertainty is that ER, temperature and precipitation are not the only

factors influencing VWC. For a more detailed consideration, factors such as soil conditions and soil type must also be taken into account. However, this becomes very complex quickly, as all parameters need to be measured relatively frequently, at least for training the models. Training the models with a wide range of ER and VWC data to get a good estimate seems sufficient. It is worth considering whether VWC and A-ERT should be installed for many areas to be monitored for a period of time - in order to collect enough training data - with the VWC sensors removed after the training period if the deviations have reduced sufficiently.

5.5 Active layer development throughout seasonal changes

A clear change is visible only from the beginning of October. This is reasonable because only the transition from water to ice causes a large change in ER and at this point the temperatures dropped drastically, yielding freezing of the topmost layer. This is enhanced in the following weeks. The measurements would have had to be continued to see an even more drastic increase in total ER. It is plausible that this would have occurred one week or two weeks after the end of the survey, as air temperatures were consistently around -5°C .

6 Summary and Outlook

Due to the extreme changes in the climate, especially in arctic permafrost soil regions, landslides are becoming increasingly likely on steep slopes [22]. Permafrost soil observations distinguished active layer depths and their seasonal development. This work helps to improve the assessment of VWC as a key parameter for estimating landslide risk. Random forest models were trained to estimate and predict VWC on the basis of ER measurements as well as air temperature and precipitation. Depth-dependent delaying ER, temperature and precipitation led to further error reductions below MRE of 2.8%. It was shown that VWC can be reliably estimated and predicted from ER for the location the models were trained on. Local variations resulted in great deviations because the ER validation data located outside of the training data range. Moreover, estimation of VWC from ERT revealed significant deficits.

The implementation of an automated-ERT (A-ERT) system and training of the models on ERT data at various locations is expected to eliminate these differences. This allows the ER sensors to be neglected and the training, test and validation data to be acquired using the same measurement method. By training on various sites, the different correlations between ER and VWC due to other parameters such as porosity and soil type are learned. At the beginning of October, 49 rectangular electrodes, with one meter spacing, were buried in the ground at study site 2 and connected with cables. The instrument was first deployed on 7 November 2024, after the final components had been received and integrated (Fig. 24). The initial preliminary data appears to be promising, indicating that more accurate predictions can be anticipated by next summer.

For further model improvements, it is recommended to install VWC sensors at much more depths at study site 2 next to the A-ERT. Moreover, it could be beneficial to ensure a coverage of a broader ER range to be sure that the validation data is not outside the training parameters. This could be achieved by including different sites with varying ER and VWC ranges in one model. Furthermore, hidden parameters influencing the ER-VWC correlation would be incorporated in a broader range.

Finally, an introduction of the gained relation between ER and VWC can be interpreted as a first step towards a sophisticated landslide risk hazard assessment. Following investigations could include parameters soil structures and pore water.



Figure 24: Installation of the A-ERT at study site 2 in the beginning of October (left) and instrument deployment early November (right).

Bibliography

- [1] Mika Rantanen, Alexey Yu Karpechko, Antti Lipponen, Kalle Nordling, Otto Hyvärinen, Kimmo Ruosteenoja, Timo Vihma, and Ari Laaksonen. The arctic has warmed nearly four times faster than the globe since 1979. *Communications earth & environment*, 3(1):168, 2022.
- [2] Marius Opsanger Jonassen, Hanne Hvidtfeldt Christiansen, Aleksey Shestov, and Knut Ivar Lindland Tveit. Improved monitoring and prediction of permafrost climate change related landsliding in the arctic. Technical report, Copernicus Meetings, 2023.
- [3] Oleg A. Anisimov and Frederick E. Nelson. Permafrost distribution in the northern hemisphere under scenarios of climatic change. *Global and Planetary Change*, 14(1):59–72, 1996.
- [4] HH Christiansen, JH Akerman, and Y Repelewska-Pekalowa. Active layer dynamics in greenland, svalbard and sweden. In *Extended abstract for the 8th International Permafrost Conference, Zurich*, pages 19–20, 2003.
- [5] MultiMedia LLC. Permameteocommunity. <https://www.unis.no/project/permameteocommunity/#:~:text=The%20interdisciplinary%20scientific%20PermaMeteoCommunity%20project,meteorological%20climate%20change%20response%20system.>, 2024. Accessed: 2024-07-26.
- [6] Klaus Knödel, Heinrich Krummel, and Gerhard Lange. *Handbuch zur Erkundung des Untergrundes von Deponien und Altlasten: Band 3: Geophysik*. Springer-Verlag, 2013.
- [7] Fansong Meng, Jinguo Wang, Yongsheng Zhao, and Zhou Chen. Quantification of soil water content by machine learning using enhanced high-resolution ert. *Journal of Hydrology*, page 131994, 2024.
- [8] Teddi Herring, Antoni G Lewkowicz, Christian Hauck, Christin Hilbich, Coline Mollaret, Greg A Oldenborger, Sebastian Uhlemann, Mohammad Farzamian, Fabrice Calmels, and Riccardo Scandroglio. Best practices for using electrical resistivity tomography to investigate permafrost. *Permafrost and Periglacial Processes*, 34(4):494–512, 2023.

- [9] Adrian Wicki and Christian Hauck. Monitoring critically saturated conditions for shallow landslide occurrence using electrical resistivity tomography. *Vadose Zone Journal*, 21(4):e20204, 2022.
- [10] Y Melvær, HF Aas, and A Skoglund. Terrengmodell Svalbard (S0 Terrengmodell). *Norwegian Polar Institute*, 465, 2014.
- [11] F. Van den Heuvel, C. Hübner, M. Błaszczyk, M. Heimann, and H. (eds) 2020 Lihavainen. SESS report 2019. *Svalbard Integrated Arctic Earth Observing System, Longyearbyen*, https://sios-svalbard.org/SESS_Issue2.
- [12] Ananth Ranganathan. The levenberg-marquardt algorithm. *Tutorial on LM algorithm*, 11(1):101–110, 2004.
- [13] Guojie Hu, Lin Zhao, Tonghua Wu, Xiaodong Wu, Hotaek Park, Alexander Fedorov, Yufei Wei, Ren Li, Xiaofan Zhu, Zhe Sun, et al. Spatiotemporal variations and regional differences in air temperature in the permafrost regions in the northern hemisphere during 1980–2018. *Science of the Total Environment*, 791:148358, 2021.
- [14] Thom A Bogaard and Roberto Greco. Landslide hydrology: from hydrology to pore pressure. *Wiley Interdisciplinary Reviews: Water*, 3(3):439–459, 2016.
- [15] Soňa Tomašková and Thomas Ingeman-Nielsen. Quantification of freeze–thaw hysteresis of unfrozen water content and electrical resistivity from time lapse measurements in the active layer and permafrost. *Permafrost and Periglacial Processes*, 35(2):79–97, 2024.
- [16] Lutz Schirrmeister, Christine Siegert, and Jens Strauss. Permafrost ein sensibles klimaphänomen–begriffe, klassifikationen und zusammenhänge (permafrost a sensible climate phenomenon–terms, classifications, and relationships). *Polarforschung*, 81(1):3–10, 2012.
- [17] Inger Hanssen-Bauer, EJ Førland, Hege Hisdal, Stephanie Mayer, Anne Brit Sandø, and Asgeir Sorteberg. Climate in svalbard 2100. *A knowledge base for climate adaptation*, 470, 2019.

- [18] Hanne H Christiansen, GL Gilbert, Nikita Demidov, Mauro Guglielmin, Ketil Isaksen, Marzena Osuch, and Julia Boike. Permafrost temperatures and active layer thickness in svalbard during 2017/2018 (permasval). *SESS Report 2019-The State of Environmental Science in Svalbard*, 2020.
- [19] Wojciech Dobinski. Permafrost. *Earth-Science Reviews*, 108(3):158–169, 2011.
- [20] Barbara Matthes. *Die GEOELEKTRISCHE WIDERSTANDSTOMOGRAPHIE als Methode zur Abbildung archäologischer Strukturen - Eine vergleichende methodische Studie aus Südwestdeutschland*. PhD thesis, Ruprecht-Karls-Universität Heidelberg, 2012.
- [21] Gustave E Archie. The electrical resistivity log as an aid in determining some reservoir characteristics. *Transactions of the AIME*, 146(01):54–62, 1942.
- [22] Annette I Patton, Sara L Rathburn, and Denny M Capps. Landslide response to climate change in permafrost regions. *Geomorphology*, 340:116–128, 2019.
- [23] Samuele Segoni, Luca Piciullo, and Stefano Luigi Gariano. A review of the recent literature on rainfall thresholds for landslide occurrence. *Landslides*, 15(8):1483–1501, 2018.
- [24] Meng Heng Loke and Ron D Barker. Rapid least-squares inversion of apparent resistivity pseudosections by a quasi-newton method1. *Geophysical prospecting*, 44(1):131–152, 1996.
- [25] Jens Oeser. Wahlpflichtmodul 35, Geophysikalische Datenanalyse, Geoelektrik und Elektromagnetik. <https://www.geophysik.uni-muenchen.de/~oeser/LV/GeoelektrikElektromagnetik.pdf>, 2020. Accessed: 2024-07-04.
- [26] Joseph Doetsch, Thomas Ingeman-Nielsen, Anders V Christiansen, Gianluca Fian-daca, Esben Auken, and Bo Elberling. Direct current (dc) resistivity and induced polarization (ip) monitoring of active layer dynamics at high temporal resolution. *Cold Regions Science and Technology*, 119:16–28, 2015.
- [27] M.H. Loke and R.D. Barker. Rapid least-squares inversion of apparent resistivity pseudosections by a quasi-newton method1. *Geophysical Prospecting*, 44(1):131–152, 1996.

- [28] Jean Virieux, Henri Calandra, and René-Édouard Plessix. A review of the spectral, pseudo-spectral, finite-difference and finite-element modelling techniques for geophysical imaging. *Geophysical Prospecting*, 59(Modelling Methods for Geophysical Imaging: Trends and Perspectives):794–813, 2011.
- [29] Michał Glazer, Wojciech Dobiński, Artur Marciniak, Mariusz Majdański, and Małgorzata Błaszczyk. Spatial distribution and controls of permafrost development in non-glacial arctic catchment over the holocene, fuglebekken, sw spitsbergen. *Geomorphology*, 358:107128, 2020.
- [30] Colin G. Farquharson and Douglas W. Oldenburg. Non-linear inversion using general measures of data misfit and model structure. *Geophysical Journal International*, 134(1):213–227, 07 1998.
- [31] Meng Heng Loke, Ian Acworth, and Torleif Dahlin. A comparison of smooth and blocky inversion methods in 2d electrical imaging surveys. *Exploration geophysics*, 34(3):182–187, 2003.
- [32] M.H. Loke and T. Dahlin. A comparison of the gauss–newton and quasi-newton methods in resistivity imaging inversion. *Journal of Applied Geophysics*, 49(3):149–162, 2002.
- [33] Henri P Gavin. The levenberg-marquardt algorithm for nonlinear least squares curve-fitting problems. *Department of Civil and Environmental Engineering Duke University August*, 3, 2019.
- [34] Graham Gilbert, Arne Instanes, Anatoly Sinitsyn, and Arne Aalberg. Characterization of two sites for geotechnical testing in permafrost: Longyearbyen, svalbard. 2019.
- [35] Kevin P Murphy. *Machine learning: a probabilistic perspective*. MIT press, 2012.
- [36] Leo Breiman. Random forests. *Machine learning*, 45:5–32, 2001.
- [37] Leo Breiman. Bagging predictors. *Machine learning*, 24:123–140, 1996.
- [38] GL Gilbert. Cryostratigraphy and sedimentology of high-arctic fjord-valleys (phd thesis). *Longyearbyen: University of Bergen & University Centre in Svalbard*, 2018.

- [39] Hanne H. Christiansen, Graham L. Gilbert, Ullrich Neumann, Nikita Demidov, Mauro Guglielmin, Ketil Isaksen, Marzena Osuch, and Julia Boike. Ground ice content, drilling methods and equipment and permafrost dynamics in Svalbard 2016–2019 (PermaSval), January 2021.
- [40] Ole Humlum. Holocene permafrost aggradation in svalbard. *Geological Society, London, Special Publications*, 242(1):119–129, 2005.
- [41] Line Rouyet, Tom Rune Lauknes, Hanne H Christiansen, Sarah M Strand, and Yngvar Larsen. Seasonal dynamics of a permafrost landscape, adventdalen, svalbard, investigated by insar. *Remote Sensing of Environment*, 231:111236, 2019.
- [42] Eirik J Førland, Rasmus Benestad, Inger Hanssen-Bauer, Jan Erik Haugen, and Torill Engen Skaugen. Temperature and precipitation development at svalbard 1900–2100. *Advances in meteorology*, 2011(1):893790, 2011.
- [43] Hanne H Christiansen, Wesley Farnsworth, Graham L Gilbert, Holt Hancock, Ole Humlum, Brendan O’Neill, Alexander Prokop, and Sarah M Strand. Report on the 14-15 october 2016 mass movement event in the longyearbyen area. *The University Centre in Svalbard (UNIS)*, 2016.
- [44] Eirik Albrechtsen, Martin Indreiten, and Siiri Wickström. Look to longyearbyen for climate adaptation. <https://www.unis.no/news/look-to-longyearbyen-for-climate-adaptation/>, 2022. Accessed: 2024-08-27.
- [45] Norikazu Matsuoka. Solifluction rates, processes and landforms: a global review. *Earth-Science Reviews*, 55(1-2):107–134, 2001.
- [46] Stefanie Härtel and Hanne H Christiansen. Geomorphological and Cryological Map of Adventdalen, Svalbard. *PANGAEA*, 2014.
- [47] Guillaume Blanchy, Sina Saneiyani, James Boyd, Paul McLachlan, and Andrew Binley. ResIPy, an intuitive open source software for complex geoelectrical inversion/modeling. page 104423.

- [48] Cristian Scapozza and Laetitia Laigre. The contribution of electrical resistivity tomography (ert) in alpine dynamics geomorphology: case studies from the swiss alps. *Géomorphologie: relief, processus, environnement*, 20(1):27–42, 2014.
- [49] Teddi Herring, Adam Pidlisecky, and Edwin Cey. Removing the effects of temperature on electrical resistivity tomography data collected in partially frozen ground: Limitations and considerations for field applications. *Vadose Zone Journal*, 20(5):e20146, 2021.
- [50] Neil Terry, Frederick D Day-Lewis, John W Lane Jr, Carole D Johnson, and Dale Werkema. Field evaluation of semi-automated moisture estimation from geophysics using machine learning. *Vadose Zone Journal*, 22(2):e20246, 2023.
- [51] Benjamin F Schwartz, Mazdeline E Schreiber, and Tingting Yan. Quantifying field-scale soil moisture using electrical resistivity imaging. *Journal of Hydrology*, 362(3-4):234–246, 2008.
- [52] Hamed Adab, Renato Morbidelli, Carla Saltalippi, Mahmoud Moradian, and Gholam Abbas Fallah Ghalhari. Machine learning to estimate surface soil moisture from remote sensing data. *Water*, 12(11):3223, 2020.
- [53] Sajjad Ahmad, Ajay Kalra, and Haroon Stephen. Estimating soil moisture using remote sensing data: A machine learning approach. *Advances in water resources*, 33(1):69–80, 2010.
- [54] Valdimiro Cussei. Estimation of soil moisture and earth resistivity using wenner’s method and machine learning. 2020.
- [55] Wei Cao, Yu Sheng, Jichun Wu, and Erxing Peng. Differential response to rainfall of soil moisture infiltration in permafrost and seasonally frozen ground in kangqiong small basin on the qinghai-tibet plateau. *Hydrological Sciences Journal*, 66(3):525–543, 2021.
- [56] Sergio E Serrano. Modeling infiltration with approximate solutions to richard’s equation. *Journal of Hydrologic Engineering*, 9(5):421–432, 2004.

- [57] Robert E Horton. An approach toward a physical interpretation of infiltration capacity. In *Soil science Society of America proceedings*, volume 5, page 24. Madison, 1940.
- [58] Yongwei Fu, Robert Horton, and Josh Heitman. Estimation of soil water retention curves from soil bulk electrical conductivity and water content measurements. *Soil and Tillage Research*, 209:104948, 2021.

Appendix

A Additional ERT

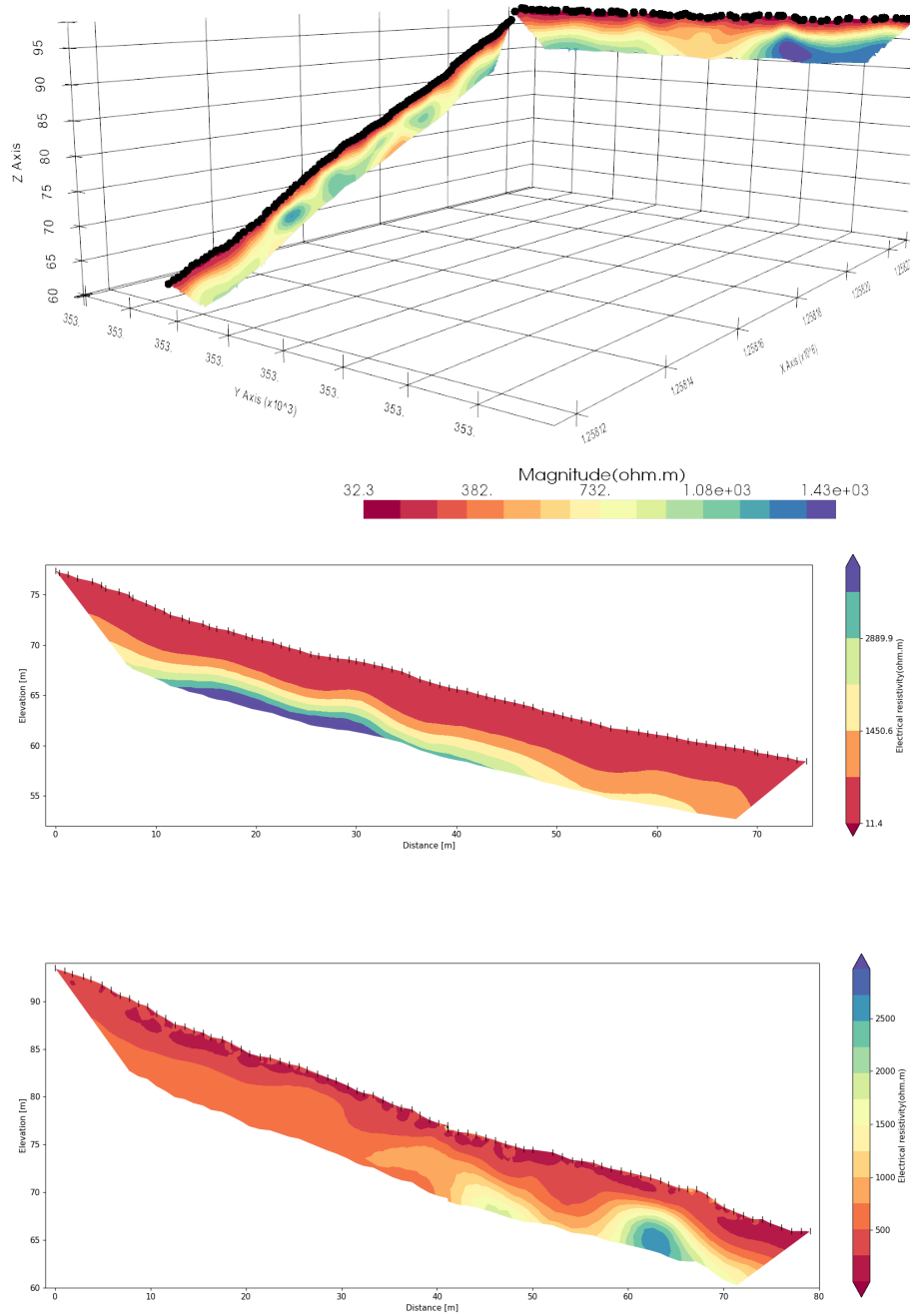


Figure A.1: Height corrected ERT of the different locations, acquired 02.-05.09.2024. The x and y axis for the 3d figure (sites 1.1 and 1.2) are cartesian coordinates. The middle ERT is site 3 and the lower one site 4.

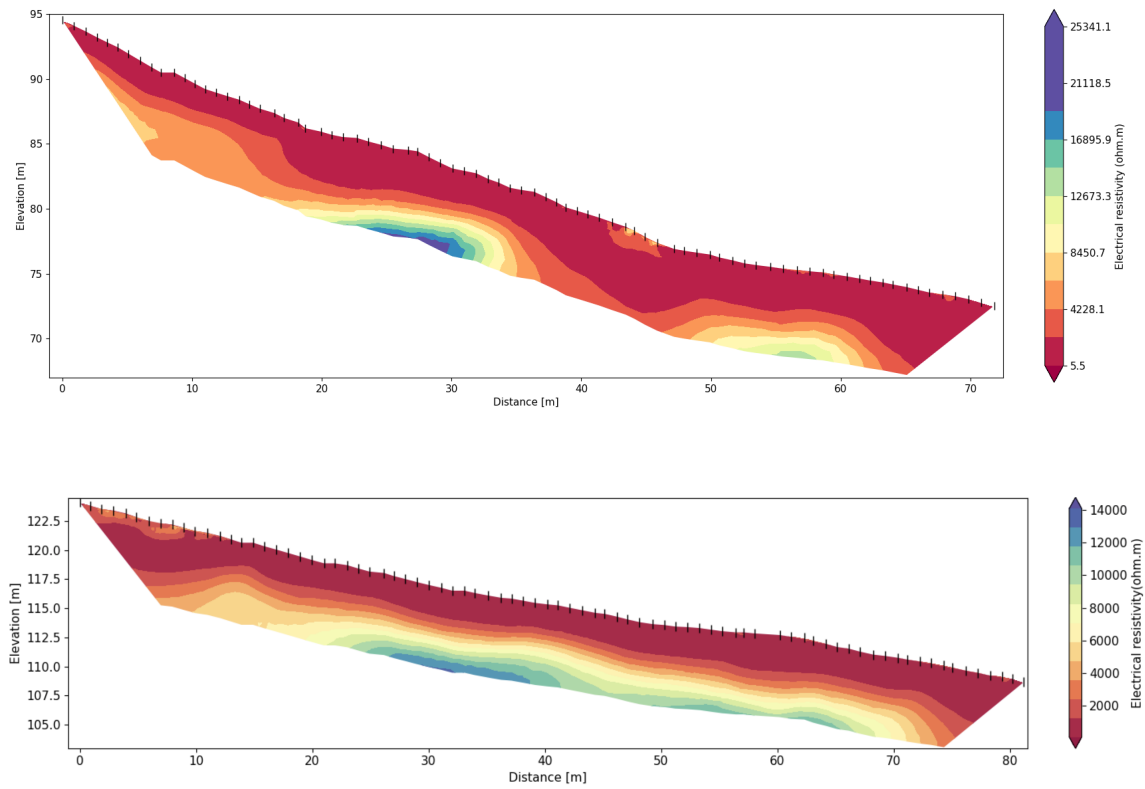


Figure A.2: Height corrected ERT of the different locations (top: 5, bottom: 6), acquired 02.-05.09.2024.

B General ERT

Table B.5: The mean electrical resistivity, standard deviation, and the relative error for every meter in depth.

Depth range (m)	Mean electrical resistivity ($\Omega \cdot m$)	Standard deviation of mean ($\Omega \cdot m$)	Relative error (%)
0.07 - 1.00	134.80	32.93	24.43
1.00 - 2.00	223.20	90.32	40.47
2.00 - 3.00	620.81	251.44	40.50
3.00 - 4.00	1315.15	408.92	31.09
4.00 - 5.00	2121.48	507.97	23.94
5.00 - 6.00	2822.26	517.37	18.33
6.00 - 7.36	3341.14	486.65	14.57

Table B.6: Electrical resistivity means dynamically calculated with a relative error of 20%. In addition, a constraint of a minimum depth range of 5 cm was applied. The blue rows indicate significantly larger depth ranges with similar large errors.

Depth range (m)	Mean electrical resistivity ($\Omega \cdot m$)	Standard deviation of mean ($\Omega \cdot m$)	Relative error (%)
-7.36 - -4.66	3017.44	605.64	20.07
4.66 - 4.61	2236.11	469.81	21.01
4.61 - 4.56	2195.30	468.35	21.33
4.56 - 4.51	2154.68	465.23	21.59
4.51 - 4.46	2115.28	459.05	21.70
4.46 - 4.41	2071.59	455.72	22.00
4.41 - 4.36	2029.57	450.78	22.21
4.36 - 4.31	1994.68	444.64	22.29
4.31 - 4.26	1951.66	439.49	22.52
4.26 - 4.21	1908.48	434.88	22.79
4.21 - 4.16	1867.81	428.00	22.91
4.16 - 4.11	1825.26	422.40	23.14
4.11 - 4.06	1782.35	417.65	23.43
4.06 - 4.01	1741.64	410.39	23.56
4.01 - 3.96	1705.52	404.79	23.73
3.96 - 3.91	1661.92	399.31	24.03
3.91 - 3.86	1620.77	391.48	24.15
3.86 - 3.81	1578.66	384.22	24.34
3.81 - 3.76	1535.70	377.66	24.59
3.76 - 3.71	1494.94	369.67	24.73
3.71 - 3.66	1453.79	361.61	24.87
3.66 - 3.61	1416.59	356.28	25.15
3.61 - 3.56	1376.06	348.44	25.32
3.56 - 3.51	1335.54	340.15	25.47

Continued on next page

Depth range (m)	Mean electrical resistivity ($\Omega \cdot m$)	Standard deviation of mean ($\Omega \cdot m$)	Relative error (%)
3.51 - 3.46	1293.61	333.58	25.79
3.46 - 3.41	1253.66	325.73	25.98
3.41 - 3.36	1214.36	318.03	26.19
3.36 - 3.31	1173.71	311.17	26.51
3.31 - 3.26	1140.80	304.63	26.70
3.26 - 3.21	1103.00	296.72	26.90
3.21 - 3.16	1063.78	289.61	27.22
3.16 - 3.11	1026.36	282.01	27.48
3.11 - 3.06	989.83	273.85	27.67
3.06 - 3.01	957.81	267.40	27.92
3.01 - 2.96	921.53	259.76	28.19
2.96 - 2.91	886.54	251.30	28.35
2.91 - 2.86	851.18	243.59	28.62
2.86 - 2.81	816.69	235.69	28.86
2.81 - 2.76	783.39	227.64	29.06
2.76 - 2.71	749.78	219.68	29.30
2.71 - 2.66	721.24	212.86	29.51
2.66 - 2.61	689.13	204.70	29.70
2.61 - 2.56	657.39	196.28	29.86
2.56 - 2.51	625.97	188.21	30.07
2.51 - 2.46	596.28	179.47	30.10
2.46 - 2.41	567.16	171.26	30.20
2.41 - 2.36	538.73	163.14	30.28
2.36 - 2.31	515.47	156.43	30.35
2.31 - 2.26	489.28	148.77	30.41
2.26 - 2.21	463.71	141.18	30.45
2.21 - 2.16	439.36	134.06	30.51
2.16 - 2.11	415.91	126.92	30.52
2.11 - 2.06	393.10	120.07	30.54

Continued on next page

Depth range (m)	Mean electrical resistivity ($\Omega \cdot m$)	Standard deviation of mean ($\Omega \cdot m$)	Relative error (%)
2.06 - 2.01	371.67	113.06	30.42
2.01 - 1.96	353.89	107.19	30.29
1.96 - 1.91	333.62	100.56	30.14
1.91 - 1.86	314.57	94.16	29.93
1.86 - 1.81	296.68	88.56	29.85
1.81 - 1.76	279.58	83.00	29.69
1.76 - 1.71	263.89	77.89	29.52
1.71 - 1.66	249.71	72.77	29.14
1.66 - 1.61	238.79	68.61	28.73
1.61 - 1.56	227.23	63.77	28.06
1.56 - 1.51	216.44	59.15	27.33
1.51 - 1.46	206.27	54.81	26.57
1.46 - 1.41	196.56	50.52	25.70
1.41 - 1.36	187.55	46.59	24.84
1.36 - 1.31	179.07	42.70	23.84
1.31 - 1.26	172.29	39.49	22.92
1.26 - 1.21	165.16	36.02	21.81
1.21 - 1.16	158.79	32.88	20.70
1.16 - 0.31	135.27	27.67	20.46
0.31 - 0.26	139.44	41.55	29.80
0.26 - 0.21	141.35	44.22	31.28
0.21 - 0.16	142.87	46.64	32.65
0.16 - 0.11	143.92	48.46	33.67
0.11 - 0.07	145.73	48.70	33.41

Table B.7: Electrical resistivity, standard deviation (Std), and relative error for different sensor depths of S 2.1.

Sensor (x, depth) (m)	Electrical resistivity ($\Omega \cdot m$)	Std deviation ($\Omega \cdot m$)	Relative error (%)
(25.75, -0.1)	108.61	5.36	4.93
(25.75, -0.5)	109.46	3.58	3.27
(25.75, -1.0)	123.41	11.12	9.01
(25.75, -1.5)	230.24	24.71	10.73
(25.75, -1.9)	333.10	78.16	23.46

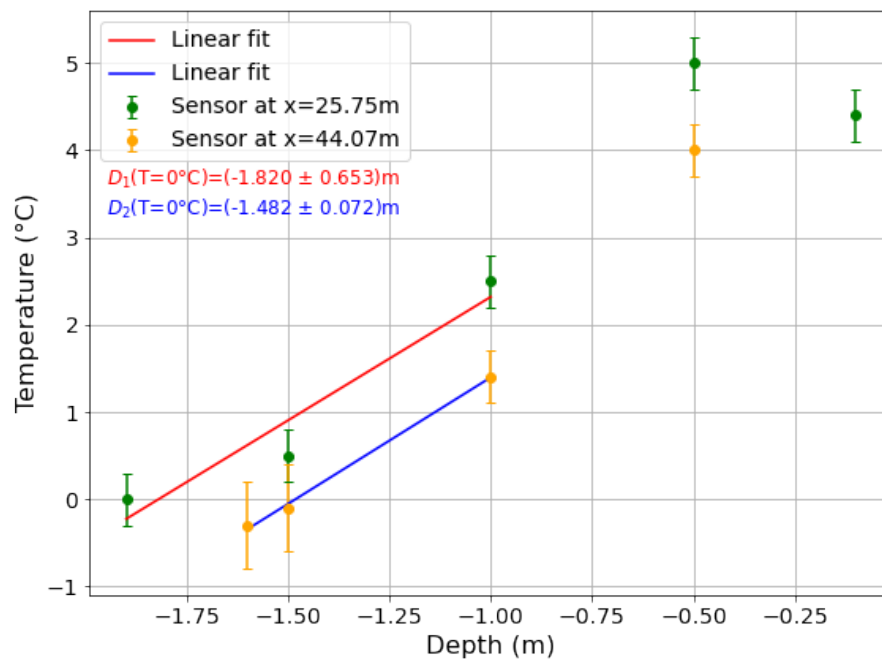


Figure B.3: The temperature calibration of the ERT in the general ERT analysis (ERT ID 2, 28.08.2024). Here, the temperatures of the sensors S 2.1 are interpolated to find the depth at which the temperature reaches 0 °C.

C Correlating VWC and ER

Table C.8: Searching for the best delay parameters for each depths and combination of delays between 0 and 72 h.

Depth (cm)	Observation period (h)	Delay _R (h)	Delay _T (h)	Delay _P (h)	MAE (10^{-4}) $cm^3 cm^{-3}$	Relative error (%)
10	0-72	0	6	42	26.87	0.00
10	6-72	6	12	48	30.96	15.21
10	12-72	12	72	18	36.23	34.81
10	18-72	18	18	18	39.50	46.99
10	24-72	24	24	24	41.99	56.26
10	30-72	30	30	30	47.34	76.16
10	36-72	48	36	42	51.03	89.87
10	42-72	72	54	42	55.01	104.69
10	48-72	54	54	48	60.24	124.14
50	0-72	36	18	60	29.89	0.00
50	6-72	36	18	60	29.89	0.00
50	12-72	36	18	60	29.89	0.00
50	18-72	36	18	60	29.89	0.00
50	24-72	48	24	54	30.88	3.32
50	30-72	72	30	42	31.62	5.82
50	36-72	48	54	72	33.24	11.22
50	42-72	48	54	72	33.24	11.22
50	48-72	48	54	72	33.24	11.22
100	0-72	0	0	18	30.23	0.00
100	6-72	18	18	36	32.72	8.23
100	12-72	18	18	36	32.72	8.23
100	18-72	18	18	36	32.72	8.23
100	24-72	30	42	24	38.54	27.48
100	30-72	30	42	36	42.40	40.24
100	36-72	66	72	54	44.52	47.27
100	42-72	66	72	54	44.52	47.27

Continued on next page

Depth (cm)	Observation period (h)	Delay _R (h)	Delay _T (h)	Delay _P (h)	MAE (10^{-4}) $cm^3 cm^{-3}$	Relative error (%)
100	48-72	66	72	54	44.52	47.27
150	0-72	0	30	24	15.73	0.00
150	6-72	6	36	24	16.86	7.15
150	12-72	30	36	42	20.21	28.47
150	18-72	30	36	42	20.21	28.47
150	24-72	30	36	42	20.21	28.47
150	30-72	30	36	42	20.21	28.47
150	36-72	54	42	72	23.66	50.39
150	42-72	54	42	72	23.66	50.39
150	48-72	54	60	72	25.20	60.17
190	0-72	36	18	54	8.12	0.00
190	6-72	36	18	54	8.12	0.00
190	12-72	36	18	54	8.12	0.00
190	18-72	36	18	54	8.12	0.00
190	24-72	54	66	24	8.14	0.30
190	30-72	54	66	36	8.44	3.93
190	36-72	54	66	36	8.44	3.93
190	42-72	66	60	66	8.44	3.94
190	48-72	66	60	66	8.44	3.94

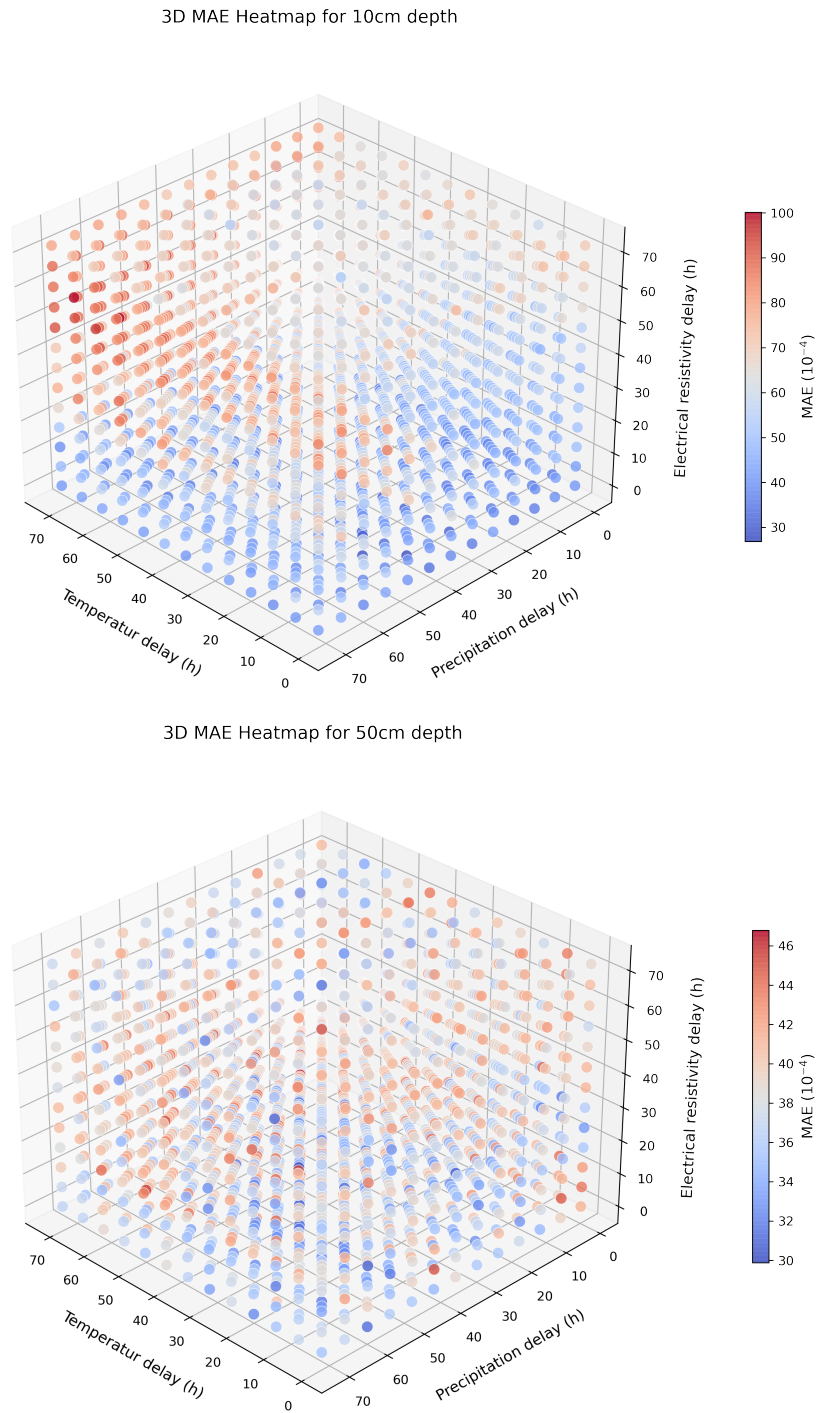
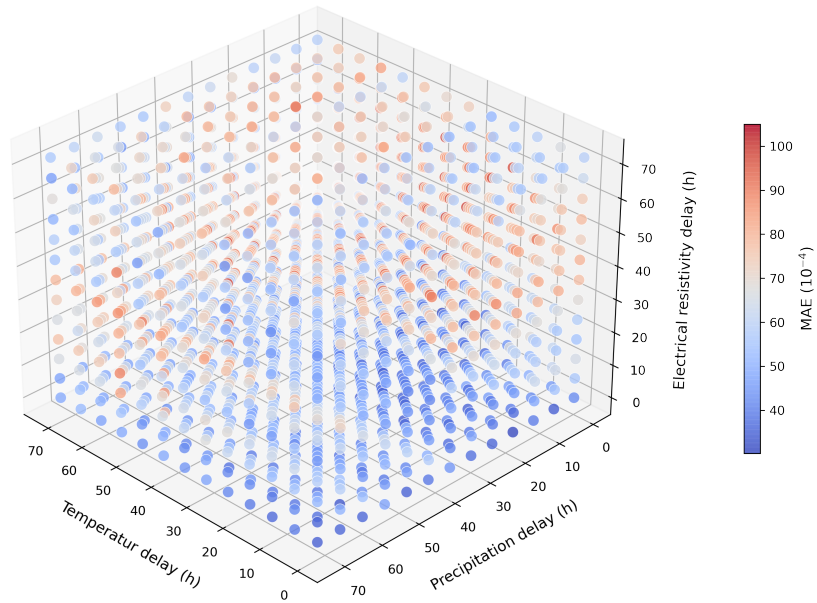


Figure C.4: MAE depending on delay times for ER, air temperature and precipitation at depth of 10 c and 50 cm.

3D MAE Heatmap for 100cm depth



3D MAE Heatmap for 150cm depth

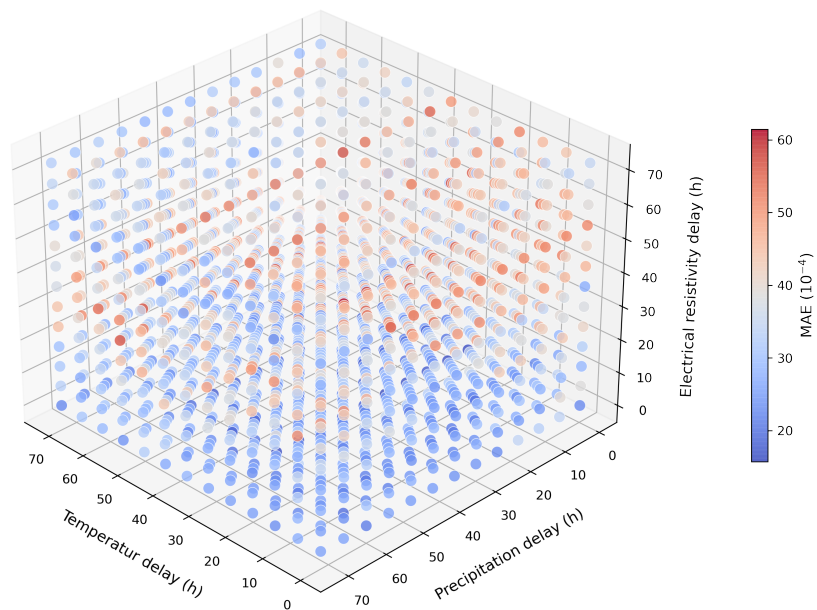


Figure C.5: MAE depending on delay times for ER, air temperature and precipitation at depth of 100 cm and 150 cm.

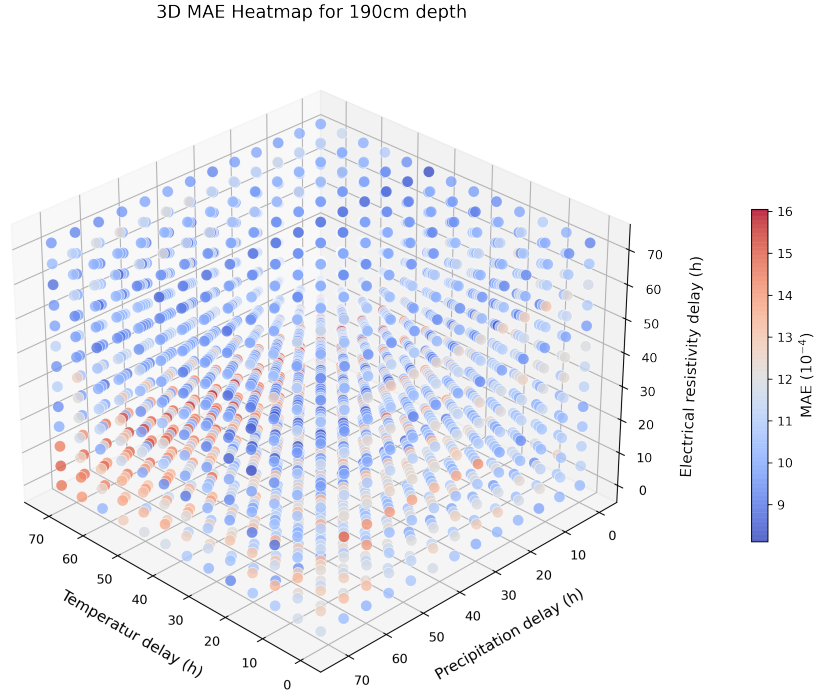


Figure C.6: MAE depending on delay times for ER, air temperature and precipitation at depth of 190 cm.

Table C.9: Delay parameters for the best VWC estimation, the electrical resistivity is left without any delay for all depths. For the delay time 'R' indicates electrical resistivity, 'T' stands for the air temperature and 'P' is precipitation.

Depth	10 cm	50 cm	100 cm	150 cm	190 cm
Delay _R (h)	0	0	0	0	0
Delay _T (h)	6	0	0	30	36
Delay _P (h)	42	60	18	24	12
MAE ($10^{-4} \text{cm}^3 \text{cm}^{-3}$)	26.9	31.1	30.2	15.7	8.6

Table C.10: Delay parameters and mean absolute error for the best VWC 24 h forecast.

Depth	10 cm	50 cm	100 cm	150 cm	190 cm
Delay _R (h)	24	48	30	30	54
Delay _T (h)	24	24	42	36	66
Delay _P (h)	24	54	24	42	24
MAE ($10^{-4} \text{cm}^3 \text{cm}^{-3}$)	42.0	30.9	38.5	20.2	8.1

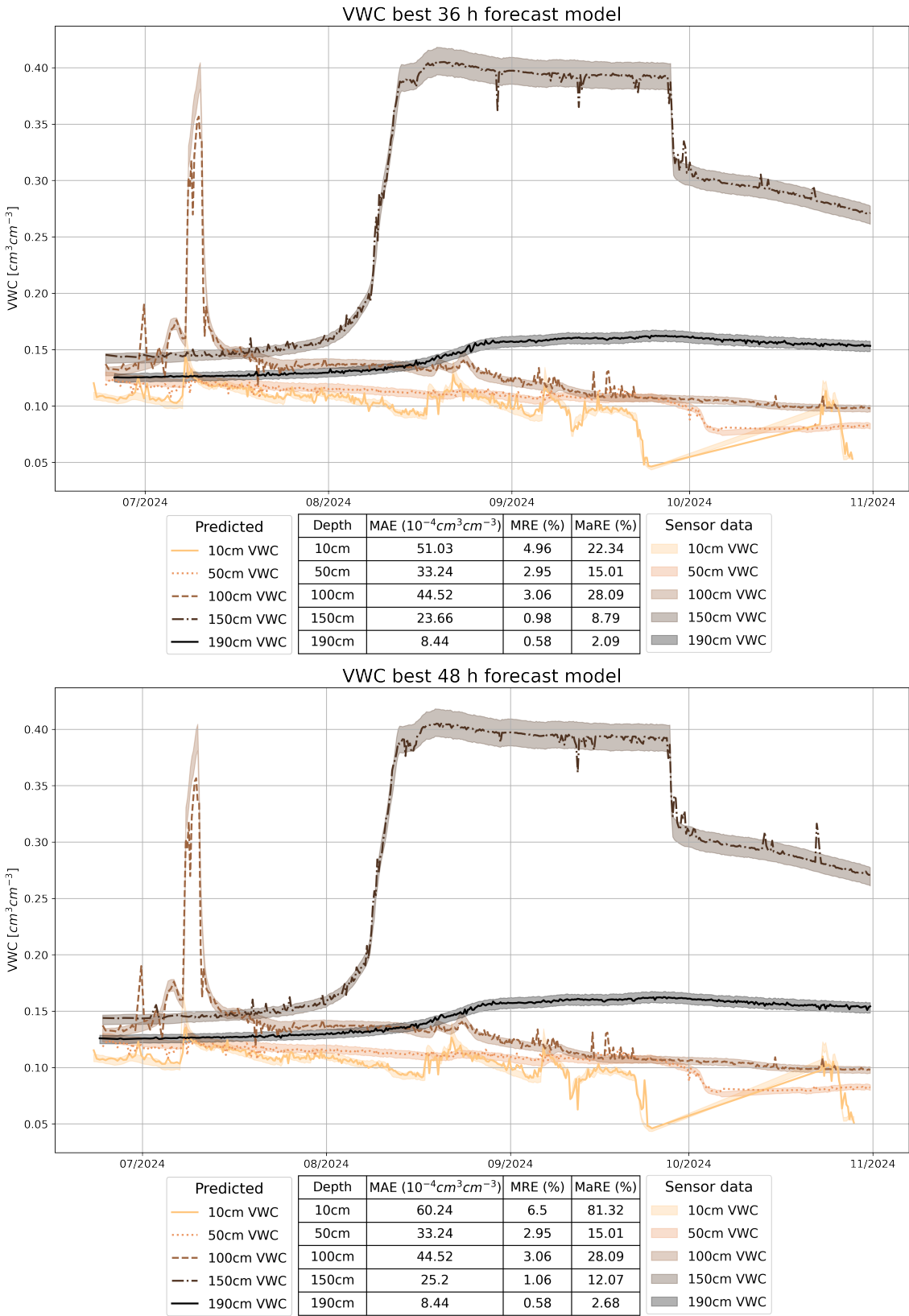


Figure C.7: Model and evaluation metrics of best 36 h and 48 h VWC forecast.

Table C.11: Upper part: Depth-dependent VWC measurements, estimations and predictions from sensors and ERT; lower part: comparisons between the estimations and predictions to the true measured values with the VWC sensors; est. means estimation and pred. describes the predictions.

Depth (cm)	VWC sensor ($\text{cm}^3\text{cm}^{-3}$)	VWC sensor error ($\text{cm}^3\text{cm}^{-3}$)	ER sensor est. ($\text{cm}^3\text{cm}^{-3}$)	ER sensor pred. ($\text{cm}^3\text{cm}^{-3}$)	ERT est. ($\text{cm}^3\text{cm}^{-3}$)	ERT pred. ($\text{cm}^3\text{cm}^{-3}$)
10	0.1041	0.0031	0.1057	0.1085	0.1472	0.1263
50	0.1102	0.0033	0.1096	0.1148	0.1280	0.1168
100	0.1249	0.0037	0.1234	0.1215	0.2720	0.1524
150	0.3977	0.0119	0.3982	0.3969	0.2948	0.3007
190	0.1556	0.0047	0.1563	0.1574	0.1566	0.1573

Deviation to VWC sensor				
Depth (cm)	ER sensor est. (σ)	ER sensor pred. (σ)	ERT est. (σ)	ERT pred. (σ)
10	0.5	1.4	14	7
50	0.18	1.4	5	2.0
100	0.4	0.9	39	7
150	0.04	0.07	9	8
190	0.14	0.4	0.20	0.4

D Short-term temporal variations

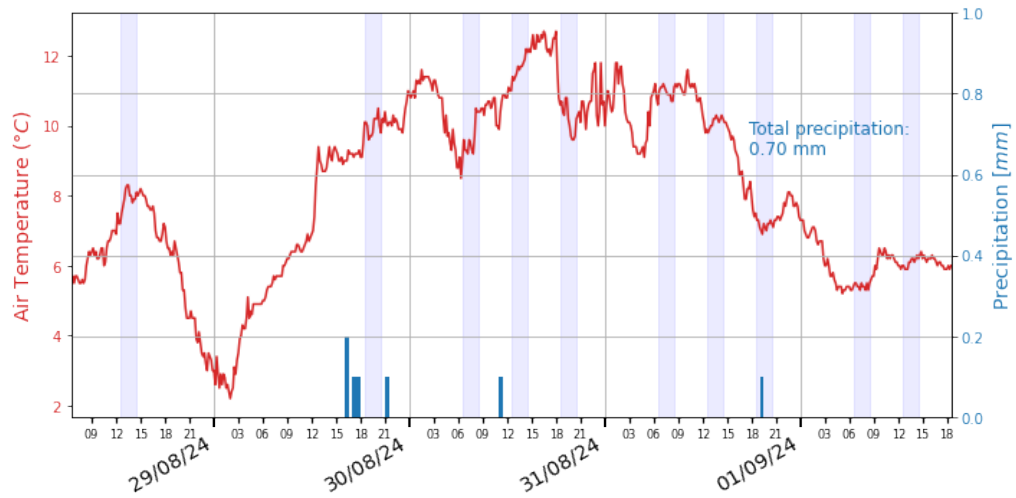


Figure D.8: Air temperature and precipitation between the measurement interval (28.08.-01.09.2024) for short-term temporal variations without heavy rainfall. The shaded regions symbolize the ERT measurement times.

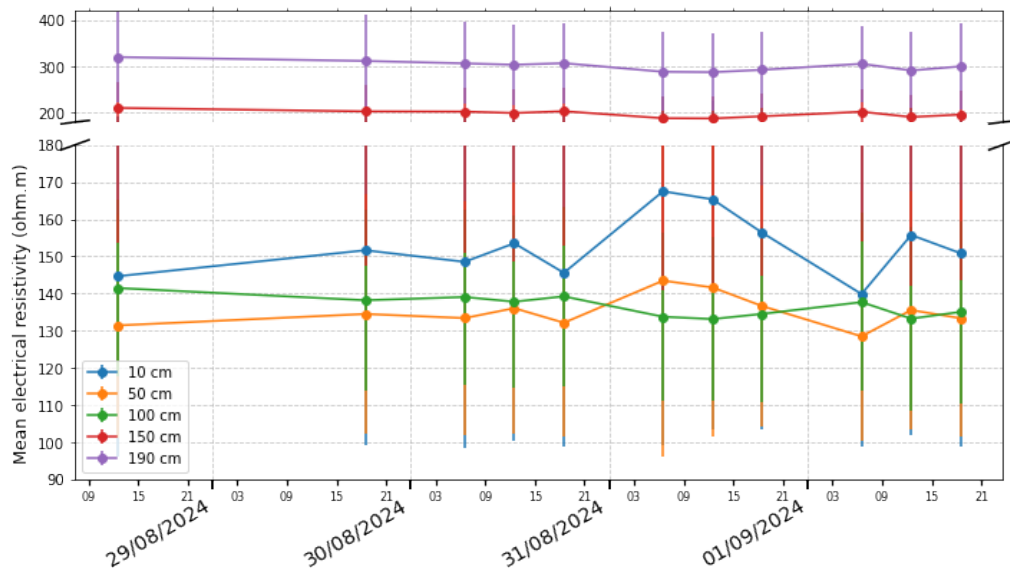


Figure D.9: The mean electrical resistivity development at the sensor points ($\pm 5\text{cm}$) without heavy rainfall.

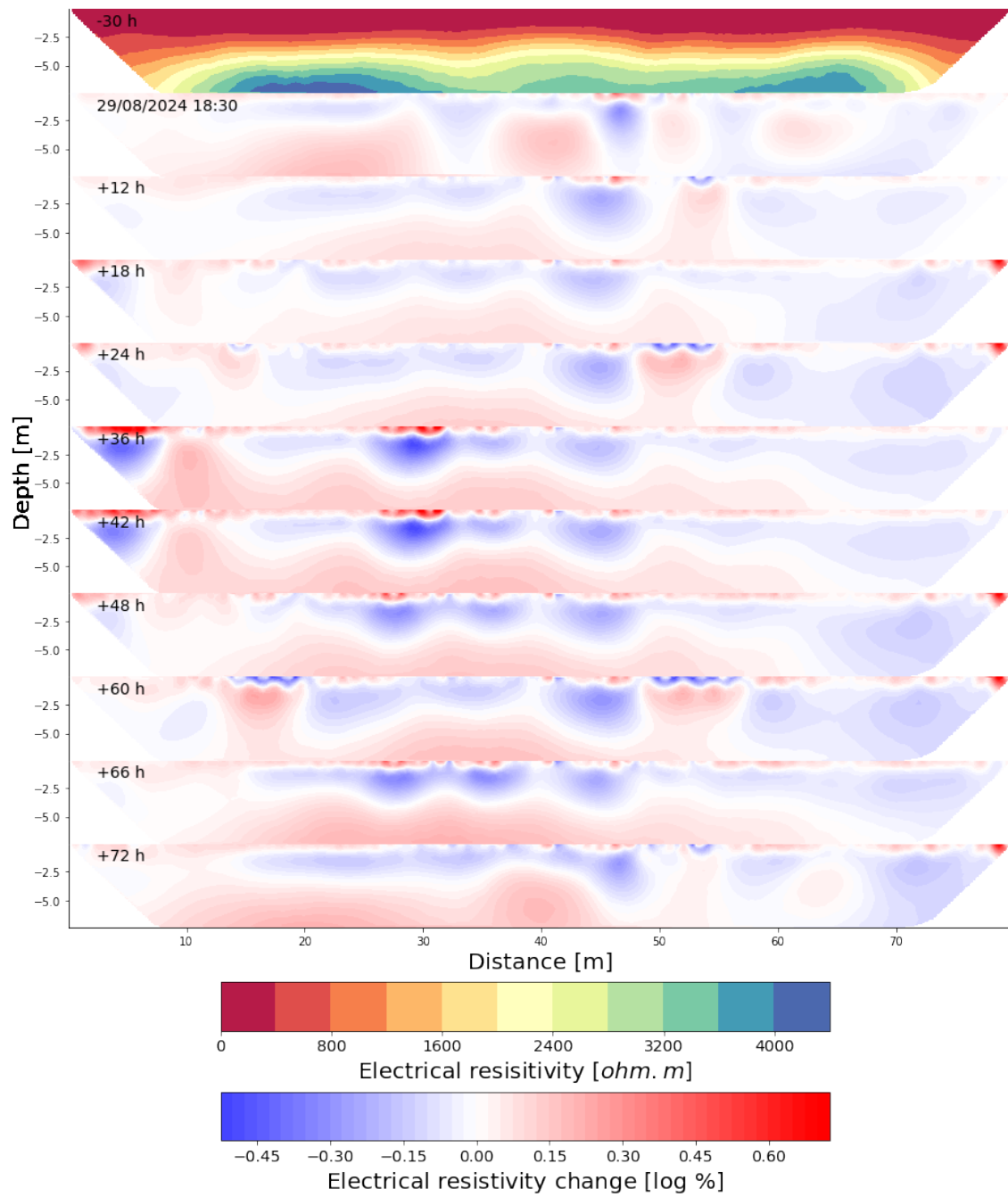


Figure D.10: Top: The acquired ERT as a reference measurement (Ref), Following: the logarithmic change ($\log(ER)/\log(Ref)$) between subsequent measurements and the reference.

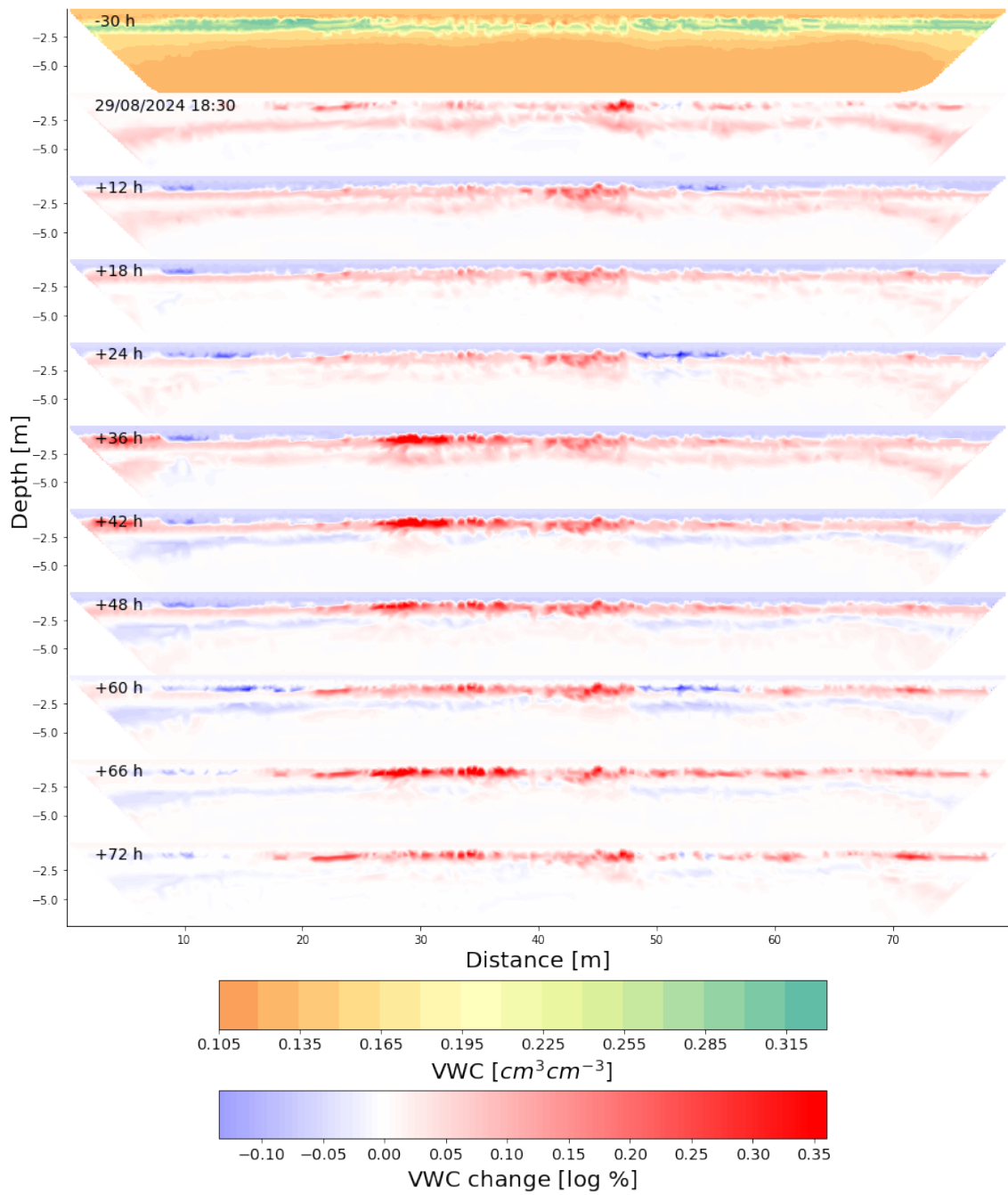


Figure D.11: Top: The VWC estimation of the first ERT as a reference measurement (Ref), Following: the logarithmic change ($\log(ER)/\log(Ref)$) between subsequent measurements and the reference. There is no heavy rainfall in between.

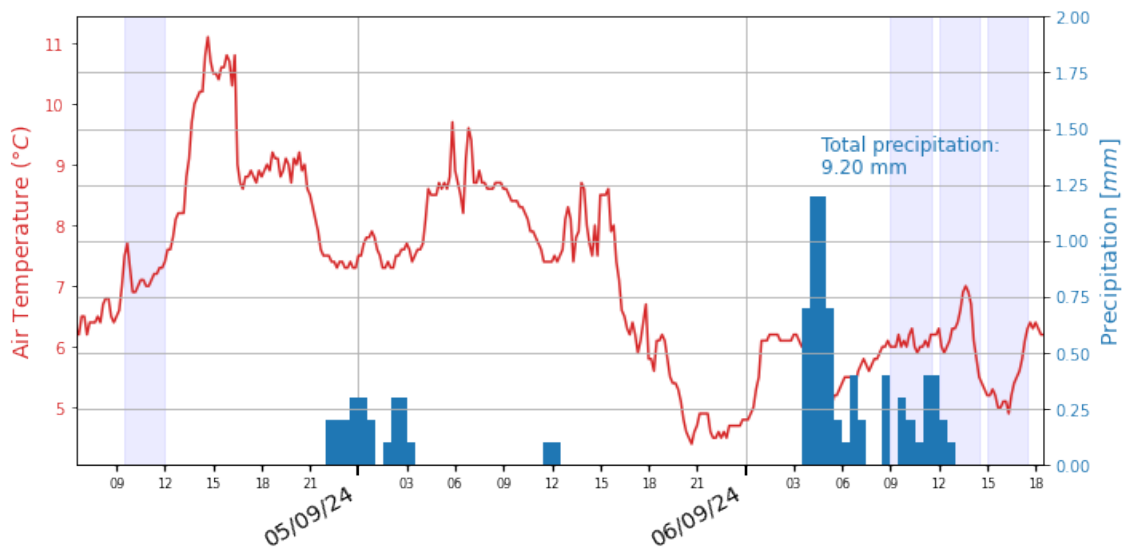


Figure D.12: Air temperature and precipitation between the measurement interval (04.09.-06.09.2024) for short-term temporal variations with heavy rainfall.

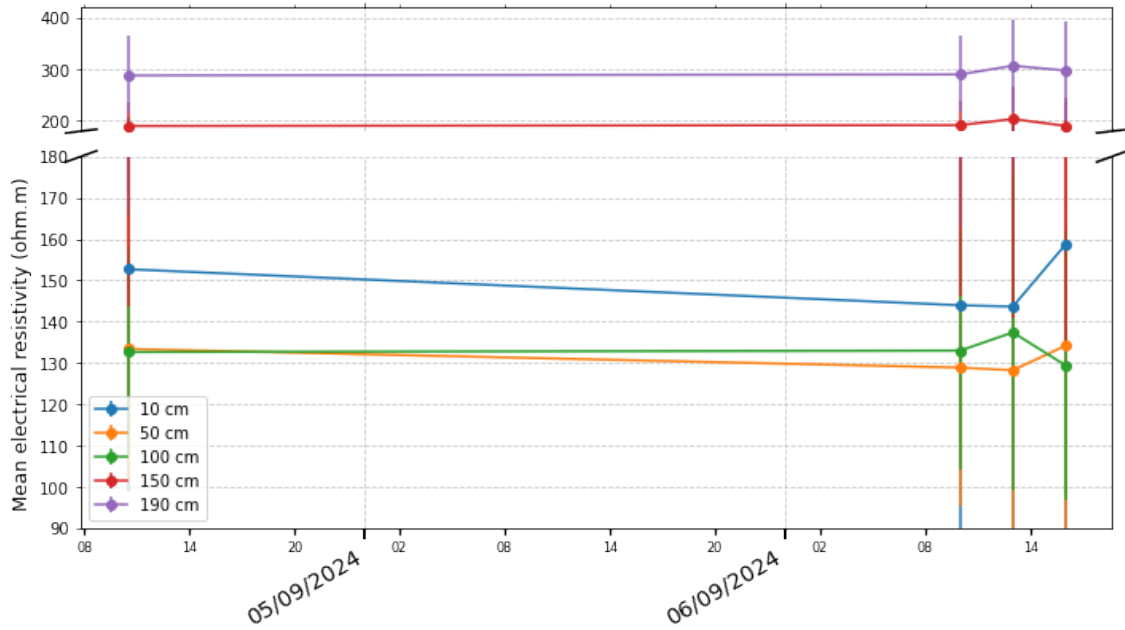


Figure D.13: The mean electrical resistivity development at the sensor points ($\pm 5\text{cm}$) with heavy rainfall. The shaded regions symbolize the ERT measurement times.

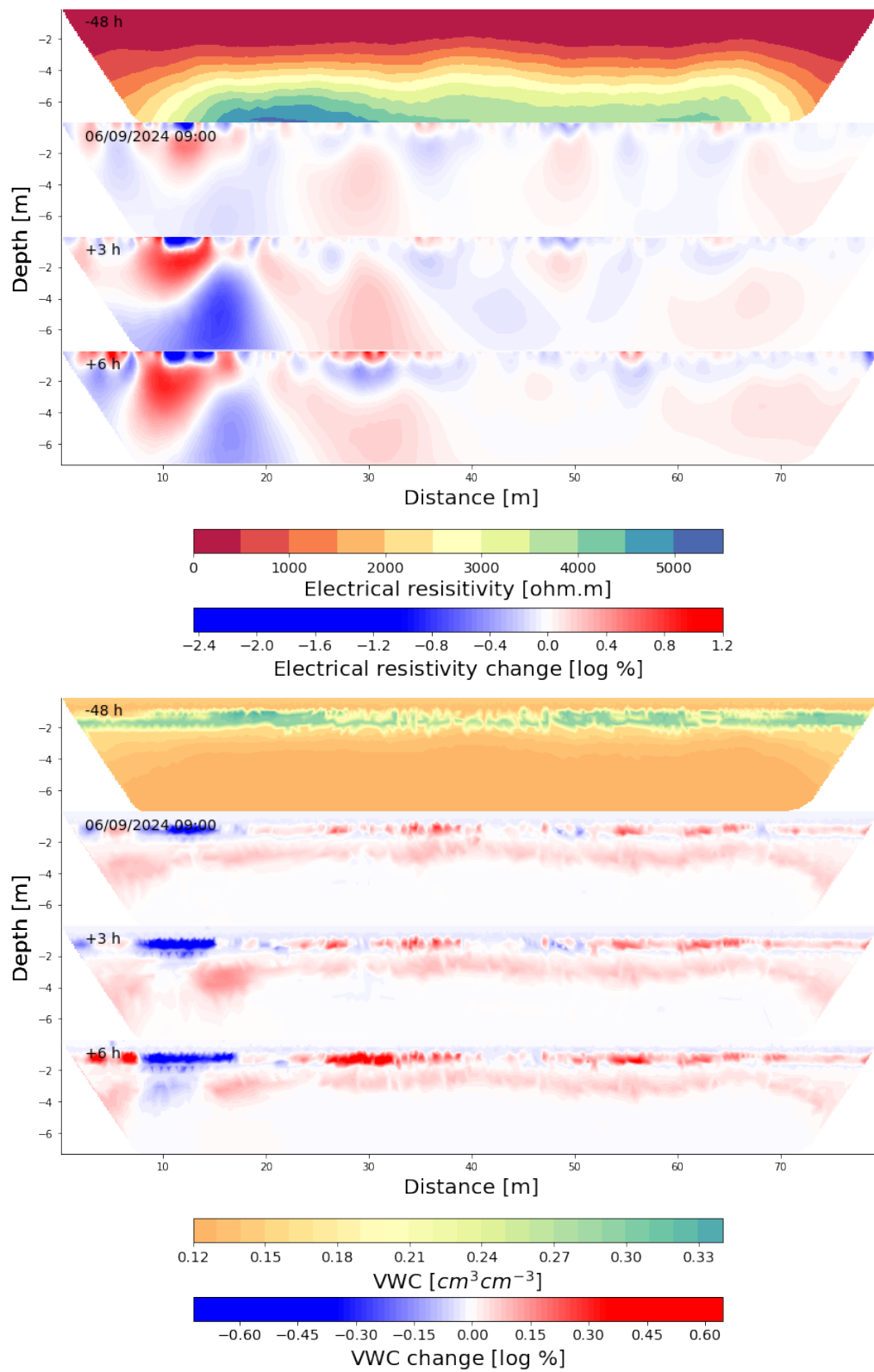


Figure D.14: Top: The acquired ERT as a reference measurement (Ref) and the logarithmic change ($\log(ER)/\log(Ref)$) between subsequent measurements and the reference. Bottom: The VWC estimation of the first ERT as a reference measurement (Ref) and the logarithmic change ($\log(VWC)/\log(Ref)$) between subsequent measurements and the reference. There is heavy rainfall in between.

E Spatial variations

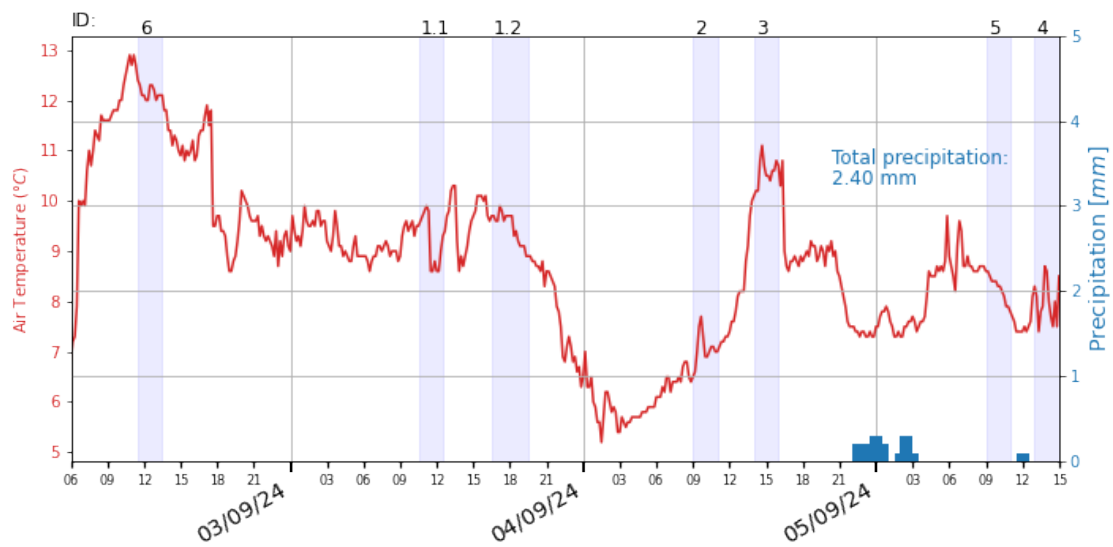


Figure E.15: Air temperature and precipitation between the measurement interval (02.09.-05.09.2024) for spatial variations. The IDs and shaded areas depict respective duration ERT recording duration.

F Long-term temporal variations

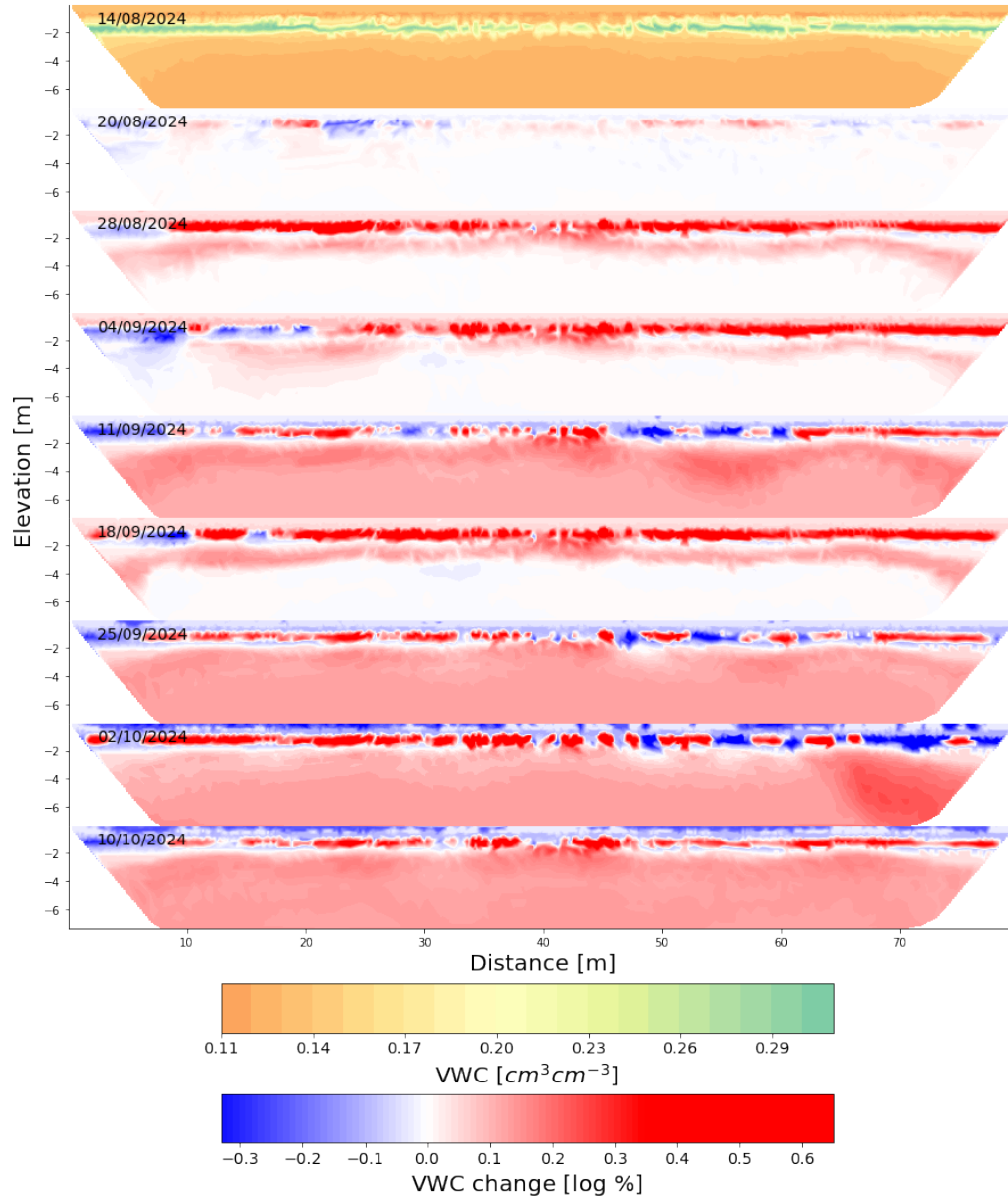


Figure F.16: The VWC estimation of the first ERT as a reference measurement (Ref) and the logarithmic change ($\log(VWC)/\log(Ref)$) between subsequent measurements and the reference.